



A flexible fully nonlinear potential flow model for wave propagation over the complex topography of the Norwegian coast

Weizhi Wang^{a,*}, Csaba Pákozdi^b, Arun Kamath^a, Sébastien Fouques^b, Hans Bihs^a

^a Norwegian University of Science and Technology, Høgskoleringen 7A, 7491 Trondheim, Norway

^b SINTEF Ocean, Otto Nielsens vei 10, 7052 Trondheim, Norway

ARTICLE INFO

Keywords:

Fully nonlinear potential flow
Coastal wave simulation
Varying bathymetry
Irregular coastline

ABSTRACT

Coastal wave propagation and transformation are complicated due to the significant variations of water depth and irregular coastlines, which are typically present at the Norwegian fjords. A potential flow model provides phase-resolved solutions with low demands on computational resources. Many potential flow models are developed for offshore waves and lack of numerical treatments of coastal conditions. In the presented work, several modifications are introduced to a fully nonlinear potential flow model with a σ -grid for the purpose of coastal wave modelling: Shallow water breaking criteria are included in addition to deepwater breaking algorithms to approximate breaking waves over a complete range of water depth. A new coastline algorithm is introduced to detect complex coastlines and ensure robust simulations near the coast. The algorithm is compatible with structured grid arrangement in the horizontal plane and allows for high-order discretisation schemes for the free surface boundary conditions for an accurate representation of complex free surfaces. A parallelised solver for the Laplace equation is utilised to ensure fast simulations for large domains with multi-core infrastructures.

The proposed model is validated against theories and experiments for various two- and three-dimensional nonlinear wave propagation and transformation cases that represent typical coastal conditions. The simulations show a good representation of nonlinear waves, and the results compare well with experiments. Furthermore, two large-scale engineering scenarios are simulated, where the applicability of the coastline algorithm and the parallel commutation capability of the model are demonstrated.

1. Introduction

The correct prediction of the wave environment is important for coastal activities such as infrastructure design, aquaculture activities and renewable energy facilities. In comparison to offshore wave fields, more complicated wave transformations take place in the coastal area due to bottom topography variations and irregular coastline geometries. The varying bathymetry influences the local wave height, either increasing it due to shoaling or reducing it due to breaking. Varying coastlines change the pattern of the wave energy propagation, either diverging the direction due to refraction and diffraction or inverting the direction due to reflection. All the complexity from wave transformations together with non-linear wave-wave interaction create an inhomogeneous wave field. As a result, a slight change of input wave height or direction leads to significant changes in local wave conditions. Therefore, it is important to examine a large area of the coastal region covering all relevant topography when efforts are made to analyse local design conditions.

It is challenging to model coastal waves with complicated irregular boundaries. Especially along the Norwegian coast, the water depth varies significantly within a short horizontal distance, usually one characteristic wavelength. The scattered archipelagos outside the fjords and the deep channels leading the swell into the fjords create strong diffraction and complicated wave-wave interactions. Widely used spectral wave models such as MIKE 21 SW (Warren and Bach, 1992) and Simulating Waves Nearshore (SWAN) (Booij et al., 1999) are capable of providing information about the wave energy distribution. However, their phase-averaging approach has a limited capacity to represent some of the nonlinear phenomena such as strong diffraction and reflection (Thomas and Dwarakish, 2015). Phased-resolved models are needed to represent wave diffraction around large obstacles.

Since the coastal waters are typically shallow in most of the coastal regions around the world, various phase-resolved shallow water equation models have been developed. Mild-slope assumptions have been

* Corresponding author.

E-mail addresses: weizhi.wang@ntnu.no (W. Wang), csaba.pakozdi@sintef.no (C. Pákozdi), arun.kamath@ntnu.no (A. Kamath), sebastien.fouques@sintef.no (S. Fouques), hans.bihs@ntnu.no (H. Bihs).

<https://doi.org/10.1016/j.apor.2022.103103>

Received 27 April 2020; Received in revised form 9 February 2022; Accepted 10 February 2022

Available online 14 March 2022

0141-1187/© 2022 The Author(s). Published by Elsevier Ltd. This is an open access article under the CC BY license (<http://creativecommons.org/licenses/by/4.0/>).

adopted and successfully used to study various coastal wave processes such as wave–current interaction (Chen et al., 2005). The significant water depth changes within one characteristic wavelength in the Norwegian fjords do not fulfil such assumptions. Boussinesq-type models (Madsen et al., 1991; Madsen and Sørensen, 1992; Nwogu, 1993) are also efficient coastal wave modelling alternatives and continuous efforts have been made to represent the dispersion relation more accurately in a deeper water condition by increasing the order of the Boussinesq dispersive terms. Wei et al. (1995) improved the dispersion relation for deeper water and enabled the model for strong non-linear interaction. This development was then incorporated into the wave model FUNWAVE (Kirby et al., 1998). Shi et al. (2012) used FUNWAVE to simulate the three-dimensional (3D) solitary wave run-up on a shelf with a conical island and achieved good agreement with the experiment by Lynett et al. (2011). Madsen and Schäffer (1998) achieved high dispersion accuracy up to dimensionless water depth to wavelength ratio $kh = 6$ (k is wave number, h is still water depth) with their high-order derivations. Similarly, a fourth-order polynomial is used in the model developed by Gobbi et al. (2000) and a faithful representation of the linear dispersion is achieved up to $kh = 6$. These methods result in up to fifth-order spatial derivatives in an extremely complex equation system, which influences the numerical instability. In addition, $kh = 6$ is not enough for many engineering applications in deepwater regions. Madsen et al. (2002) applied finite series expansions from an arbitrary z-level involving up to fifth-derivative operators and managed to represent the dispersion relation accurately up to $kh = 40$. This multiple expansion, however, results in a large set of equations and more unknowns.

Taking a different approach, Lynett and Liu (2004) divided the vertical water column into a finite number of layers with quadratic polynomials and match them at the interfaces. This multi-layer approach shows an excellent representation of linear dispersive properties up to $kh = 8$ with two layers. Further development has been presented to approximate the vertical gradient of the non-hydrostatic pressure with fewer vertical layers in deepwater (Stelling and Duinmeijer, 2003; Zijlema and Stelling, 2005, 2008; Zijlema et al., 2011). According to the reported research, the flow information in the vertical direction is sufficiently resolved with 2–3 layers in relatively deepwater conditions. However, the increase of vertical layers leads to a significant increase in computational costs. Monteban (2016) reported that a two-layer configuration results in about 10 times the computational cost in comparison to a one-layer arrangement.

Jeschke et al. (2017) presented an approach for non-hydrostatic shallow water models by introducing a quadratic pressure assumption. In this way, the model can achieve a good equivalence to a second-order Boussinesq model Jeschke et al. (2017) while avoiding the numerical instabilities due to higher-order terms in a Boussinesq-type model and the increased computational costs from a larger number of vertical layers in a multi-layer non-hydrostatic model. The effectiveness of such a method for simulating wave propagation over varying bathymetry is also shown by Wang et al. (2020b). In spite of the efforts in improving the vertical dispersion relation in shallow water equations using different methodologies, the water depth still limits the validity and applicability of such models. Other approaches based on classic Korteweg–de Vries (KdV)-type equations and the Hamiltonian structure of gravity surface waves are also explored (van Groesen et al., 2010; van Groesen and Andonowati, 2007), the resulting models are able to simulate long and short crested coastal waves over varying topography of large water depth variations.

The aforementioned numerical models are derived from the shallow water equations and utilise various techniques to improve the representation of dispersion relations in intermediate to deepwater conditions. Another approach for simulating wave propagation in deepwater conditions in a computationally efficient manner is the use of the potential flow theory. Potential flow models usually solve the Laplace equation

together with the kinematic and dynamics free surface boundary conditions and the boundary condition at the seabed. One of the most used potential flow modelling techniques is the boundary element method (BEM). Grilli et al. (1994) introduced a BEM model for wave shoaling over a slope. After a continuous development of the model (Grilli and Subramanya, 1996; Grilli and Horrillo, 1997), a fully non-linear model for three-dimensional wave propagation over arbitrary bottoms was presented and a severe breaking wave was investigated (Grilli et al., 2001). In recent developments, robust spilling breaker models have also been developed for complex surf zone dynamics (Grilli et al., 2020a,b). BEM methods are computationally efficient but mathematically demanding. The fully populated unsymmetrical matrix in a BEM model makes it difficult to implement high-order numerical schemes and parallel computation techniques. Therefore, the method is sufficient for small domain analyses but not optimal for large-scale engineering applications.

Li and Fleming (1997) presented a three dimensional fully nonlinear potential flow model with a low-order finite difference method and a multi-grid solver. The model is able to simulate nonlinear wave phenomena over a nearly complete range of water depth, however, it lacks the capacity of representing breaking waves. Based on the method, Bingham and Zhang (2007) applied higher-order numerical schemes which further improved the model's ability for representing waves of increasing nonlinearity with increasing accuracy. In a further development, Engsig-Karup et al. (2009) introduced the general-purpose fully nonlinear potential flow model OceanWave3D. The model is capable of simulating different wave transformations, including wave breaking. In addition, a GPU-accelerated version of OceanWave3D was developed (Engsig-Karup et al., 2012; Glimberg et al., 2013, 2019), which dramatically improved the computational efficiency of the model. An adaptive curvilinear grid is introduced, which offers flexibility with regard to coastal geometry. However, increasingly complex coastline geometries make curvilinear grid generation difficult and more time-consuming.

A different technique to solve for the velocity potential is the high-order spectral (HOS) method, where the Laplace equation is solved analytically in the volume beforehand. Hence, only the free surface boundary conditions need to be time-integrated, so that fewer computational resources are required. In addition, the use of Fast Fourier Transform (FFT) further increases computational efficiency. Following this methodology, several HOS models have been developed, such as HOS-NWT and HOS-Ocean (Ducrozet et al., 2012; Bonnefoy et al., 2006a,b). The models are highly effective for large-scale wave modelling in constant water depth. However, simple analytical solutions to the Laplace equation exist only for constant water depth (cosh-functions), but not for more complex bathymetries and boundary conditions. Further, certain periodic boundary conditions are required in order to efficiently apply FFT (Fructus et al., 2005). These limitations make the HOS method difficult to use for practical coastal engineering applications with irregularly varying bottom topography. In more recent efforts, a Chebyshev polynomial is used to represent the velocity potential in the vertical direction (Raoult et al., 2016; Yates and Benoit, 2015), which leads to the development of Whisper3D. The model shows more flexibility with respect to irregular topography as well as nonlinear steep and breaking waves (Zhang et al., 2019; Simon et al., 2019). Both Whisper3D and OceanWave3D show the potential for coastal wave modelling with significant wave depth changes. However, an efficient coastline algorithm is needed in order to identify wet and dry cells and to represent the coastline geometry in sufficient detail.

The complex shorelines as well as breaking wave kinematics can be represented in 3D non-hydrostatic models. In this approach, the pressure is decomposed into hydrostatic and non-hydrostatic components. Stansby and Zhou (1998) and Zhou and Stansby (1999) used the non-hydrostatic approach to solve the 3D non-hydrostatic Reynolds-averaged Navier–Stokes (RANS) equations with a surface and bottom

following a σ -coordinate grid in the vertical direction and a Cartesian grid in the horizontal direction. The non-hydrostatic pressure is solved from the Poisson equation using a conjugate gradient method. The model represents the free surface with a single-valued function. Here, the free surface is the upper boundary of the computational domain with appropriate dynamic boundary conditions on normal and tangential stresses at the top and bottom interfaces. Based on the methodology, Ma et al. (2012) presented the numerical model NHWAVE. The model represents highly nonlinear waves and features a shoreline algorithm. A wetting-drying algorithm is applied to detect the shoreline position based on a water depth threshold. The normal fluxes at cell faces are set to zero for dry cells. Though the single-valued approach does not allow for a geometric representation of an overturning wave breaker, many developments have demonstrated comprehensive wave breaking onset criteria and algorithms that represent the energy transformation during wave breaking both in deepwater and the surface zone (Derakhti et al., 2016a,b,c). Lately, a unified breaking onset criterion for surface gravity water waves in arbitrary water depth is summarised by Derakhti et al. (2020).

As discussed, shallow-water equation-based numerical wave models excel at coastal wave modelling in shallow to intermediate water depth but require special attention when the water depth becomes too large. Potential flow numerical models are ideal for deepwater wave propagation but special techniques are needed when varying bathymetry and coastlines influence the wave field. The 3D non-hydrostatic models offer breaking and coastline algorithms but are used mostly for domains of a limited extent (Grilli et al., 2020b). In order to model large-scale wave propagation along the Norwegian coast with significant water depth variations and complicated shorelines, a fast numerical model with combined features is needed.

In the presented manuscript, the fully nonlinear potential flow model REEF3D::FNPF (Bihs et al., 2020; Wang et al., 2019) is modified and adapted so that it is dedicated to coastal wave modelling in a complex coastal topographic environment. Developed as part of the open-source hydrodynamic framework REEF3D (Bihs et al., 2016), the model inherits the efficient grid generation, versatile wave generation, high-order discretisation schemes for the free surface boundary conditions and parallel computation capacity from the framework. Those numerical implementations have been shown to be robust and efficient by various applications with REEF3D::CFD. For example, three-dimensional breaking wave interaction with a vertical surface-piercing cylinder have been investigated and validated in terms of free surface elevation, wave forces, as well as velocity fields (Alagan Chella et al., 2017; Kamath et al., 2016) using REEF3D::CFD. Breaking wave interaction with multiple objects (Alagan Chella et al., 2019), complex structures (Aggarwal et al., 2020) and irregular breaking wave interaction with a mono-pile (Aggarwal et al., 2019) were also studied and validated. Furthermore, a wide range of applications and engineering scenarios have been reported using the model, including sediment transport and scour (Ahmad et al., 2019, 2020), floating structures and mooring (Martin et al., 2020) and porous coastal structure design (Sasikumar et al., 2020). The different modules within the REEF3D framework have also been inter-compared and consistent results have been shown for several benchmarks (Wang et al., 2020a). Specifically, the convective terms in the free surface boundary conditions are discretised with the 5th-order WENO scheme (Jiang and Shu, 1996) and the temporal terms are treated with the 3rd-order Runge–Kutta scheme (Shu and Osher, 1988). Parallel computation using message passing interface (MPI) and hypre's efficient parallelised geometric multi-grid solver for the Laplace equation enable fast simulations for large domains both with single-core and multi-core infrastructure. A σ -coordinate system (Engsig-Karup et al., 2009) is adopted so that the vertical grids follow the variations of the bottom topography. Various wave generation methods are implemented to maximise the flexibility, including a relaxation method, a Neumann boundary and the ability to include wave-maker signals.

The proposed model combines proven breaking wave algorithms with an innovative coastline algorithm in a computationally efficient potential flow code. The combined breaking wave algorithms detect the wave breaking events and approximate the wave energy dissipation due to wave breaking consistently over the complete range of water depths. Both a depth-based criterion (Smit et al., 2013; Zijlema et al., 2011) and a steepness-based criterion (Baquet et al., 2017) are used to determine wave breaking both in the shallow water region and the deepwater region. When wave breaking is detected, a filtering algorithm (Jensen et al., 1999) and an artificial viscous damping algorithm (Baquet et al., 2017) are used separately or in combination to dissipate wave energy. The coastline algorithm includes complicated coastlines effectively without changing the structured grid arrangement in the horizontal plane. In contrast to the curvilinear approach and multi-block methods (Engsig-Karup et al., 2009, 2012; Glimberg et al., 2013, 2019), the proposed algorithm is universally applicable instead of being case-dependent and does not require local grid refinement along the coastline. Relaxation zones are then arranged along the detected coastlines in order to reduce the numerical instability in the swash zone and customise the reflection properties of the coasts.

The manuscript is organised as follows: The governing equations, the discretisation schemes for the free surface boundary conditions, the breaking wave algorithms and coastline algorithms are elaborated in Section 2. Validations for several different scenarios of two-dimensional (2D) and three-dimensional (3D) nonlinear wave propagation and transformation are presented in Section 3. Then the model is used for large-scale applications to analyse the wave conditions at a Norwegian harbour and a fish farm site in Section 4. In the end, conclusions and outlooks of the proposed model are summarised in Section 5.

2. Numerical model

2.1. Governing equations

The governing equation for the proposed fully nonlinear potential flow model is the Laplace equation:

$$\frac{\partial^2 \phi}{\partial x^2} + \frac{\partial^2 \phi}{\partial y^2} + \frac{\partial^2 \phi}{\partial z^2} = 0. \quad (1)$$

Boundary conditions are required to solve for the velocity potential ϕ from this elliptic equation, specifically at the free surface and at the bed. The fluid particles at the free surface should remain at the surface where the pressure in the fluid should be equal to the atmospheric pressure. These conditions must be fulfilled at all times and they form the kinematic and dynamic boundary conditions at the free surface respectively:

$$\frac{\partial \eta}{\partial t} = -\frac{\partial \eta}{\partial x} \frac{\partial \tilde{\phi}}{\partial x} - \frac{\partial \eta}{\partial y} \frac{\partial \tilde{\phi}}{\partial y} + \tilde{w} \left(1 + \left(\frac{\partial \eta}{\partial x} \right)^2 + \left(\frac{\partial \eta}{\partial y} \right)^2 \right), \quad (2)$$

$$\frac{\partial \tilde{\phi}}{\partial t} = -\frac{1}{2} \left[\left(\frac{\partial \tilde{\phi}}{\partial x} \right)^2 + \left(\frac{\partial \tilde{\phi}}{\partial y} \right)^2 - \tilde{w}^2 \left(1 + \left(\frac{\partial \eta}{\partial x} \right)^2 + \left(\frac{\partial \eta}{\partial y} \right)^2 \right) \right] - g\eta. \quad (3)$$

where η is the free surface elevation, $\tilde{\phi} = \phi(\mathbf{x}, \eta, t)$ is the velocity potential at the free surface, $\mathbf{x} = (x, y)$ represents the location at the horizontal plane and \tilde{w} is the vertical velocity at the free surface.

At the bottom, the component of the velocity normal to the boundary must be zero at all times since the fluid particle cannot penetrate the solid boundary. This gives the bottom boundary condition:

$$\frac{\partial \phi}{\partial z} + \frac{\partial h}{\partial x} \frac{\partial \phi}{\partial x} + \frac{\partial h}{\partial y} \frac{\partial \phi}{\partial y} = 0, \quad z = -h, \quad (4)$$

where $h = h(x)$ is the water depth measured from the still water level to the seabed.

The Laplace equation, together with the boundary conditions are solved on a σ -coordinate system. The σ -coordinate system follows the water depth changes and offers flexibility for irregular boundaries. The

transformation from a Cartesian grid to a σ -coordinate is expressed as follows:

$$\sigma = \frac{z + h(\mathbf{x})}{\eta(\mathbf{x}, t) + h(\mathbf{x})}. \quad (5)$$

The velocity potential after the σ -coordinate transformation is denoted as Φ . The boundary conditions and the governing equation in σ -coordinates are then written in the following format:

$$\Phi = \tilde{\phi}, \quad \sigma = 1; \quad (6)$$

$$\frac{\partial^2 \Phi}{\partial x^2} + \frac{\partial^2 \Phi}{\partial y^2} + \left(\frac{\partial^2 \sigma}{\partial x^2} + \frac{\partial^2 \sigma}{\partial y^2} \right) \frac{\partial \Phi}{\partial \sigma} + 2 \left(\frac{\partial \sigma}{\partial x} \frac{\partial}{\partial x} \left(\frac{\partial \Phi}{\partial \sigma} \right) + \frac{\partial \sigma}{\partial y} \frac{\partial}{\partial y} \left(\frac{\partial \Phi}{\partial \sigma} \right) \right) + \left(\left(\frac{\partial \sigma}{\partial x} \right)^2 + \left(\frac{\partial \sigma}{\partial y} \right)^2 + \left(\frac{\partial \sigma}{\partial z} \right)^2 \right) \frac{\partial^2 \Phi}{\partial \sigma^2} = 0, \quad 0 \leq \sigma < 1; \quad (7)$$

$$\left(\frac{\partial \sigma}{\partial z} + \frac{\partial h}{\partial x} \frac{\partial \sigma}{\partial x} + \frac{\partial h}{\partial y} \frac{\partial \sigma}{\partial y} \right) \frac{\partial \Phi}{\partial \sigma} + \frac{\partial h}{\partial x} \frac{\partial \Phi}{\partial x} + \frac{\partial h}{\partial y} \frac{\partial \Phi}{\partial y} = 0, \quad \sigma = 0. \quad (8)$$

Once the velocity potential Φ is obtained in the σ -domain, the velocities can be calculated as follows:

$$u(\mathbf{x}, z) = \frac{\partial \Phi(\mathbf{x}, z)}{\partial x} = \frac{\partial \Phi(\mathbf{x}, \sigma)}{\partial x} + \frac{\partial \sigma}{\partial x} \frac{\partial \Phi(\mathbf{x}, \sigma)}{\partial \sigma}, \quad (9)$$

$$v(\mathbf{x}, z) = \frac{\partial \Phi(\mathbf{x}, z)}{\partial y} = \frac{\partial \Phi(\mathbf{x}, \sigma)}{\partial y} + \frac{\partial \sigma}{\partial y} \frac{\partial \Phi(\mathbf{x}, \sigma)}{\partial \sigma}, \quad (10)$$

$$w(\mathbf{x}, z) = \frac{\partial \Phi(\mathbf{x}, z)}{\partial z} = \frac{\partial \sigma}{\partial z} \frac{\partial \Phi(\mathbf{x}, \sigma)}{\partial \sigma}. \quad (11)$$

The Laplace equation is discretised using second-order central differences and solved using a parallelised geometric multigrid preconditioned conjugate gradient solver provided by the hypre library (van der Vorst, 1992).

The gradient terms of the free-surface boundary conditions are discretised with the 5th-order Hamilton–Jacobi version of the weighted essentially non-oscillatory (WENO) scheme (Jiang and Shu, 1996). The implementation of the WENO scheme in the presented model is described in Appendix.

For time treatment, a 3rd-order accurate total variation diminishing (TVD) Runge–Kutta scheme (Shu and Osher, 1988) is used. Adaptive time-stepping is used by controlling a constant time factor as an equivalence to the Courant–Friedrichs–Lewy (CFL) condition:

$$c_u = \frac{dx}{\left| \max(u_{max}, 1.0\sqrt{g * h_{max}} \right|}, \quad c_v = \frac{dy}{\left| \max(v_{max}, 1.0\sqrt{g * h_{max}} \right|}, \quad (12)$$

$$c_{tot} = \min(c_u, c_v),$$

$$dt = c_{tot} CFL.$$

where u_{max}, v_{max} are the maximum particle velocities in x and y directions at the free surface, h_{max} is the maximum water depth, $g = 9.81 \text{ m/s}^2$ is the gravitational acceleration.

The model is fully parallelised following the domain decomposition strategy where ghost cells are used to exchange information between adjacent domains. These ghost cells are updated with the values from the neighbouring processors via Message Passing Interface (MPI).

2.2. Vertical grid arrangement

As presented by Pakozdi et al. (2021), the required uniform vertical mesh resolution depends on the water depth and the wave period. In order to reduce the number of cells, the model utilises a non-uniform vertical grid arrangement which then influences how the dispersion relation is represented. Therefore, the constant truncation error method is introduced to optimise the stretching factor α and vertical grid (Pakozdi et al., 2021) in terms of computational speed (i.e. as few vertical grid cells as possible) and numerical accuracy (i.e. as many vertical cells as needed).

In the model, the vertical coordinates follow a stretching function so that the grid becomes denser close to the free surface:

$$\sigma_i = \frac{\sinh(-\alpha) - \sinh\left(\alpha\left(\frac{i}{N_z} - 1\right)\right)}{\sinh(-\alpha)}, \quad (13)$$

where α is the stretching factor and i and N_z stand for the index of the grid point and the total number of cells in the vertical direction.

As an example, a general description of a progressive Airy wave can be expressed as:

$$\eta(x, z, t) = A(z)B(z)\Gamma(t), \quad (14)$$

and function $A(z)$ follows:

$$A(z) = C e^{kz}, \quad (15)$$

which is governed only by the wave number k , which can be defined by the linear dispersion relationship to the wave angular frequency:

$$\omega^2 = gk, \quad (16)$$

where g is the gravity acceleration.

A correct representation of the phase velocity depends on the correct representation of the wave number. The new method is based on the assumption that a constant absolute truncation error at every vertical location can preserve the correct shape of the function $f(z)$ and yield the correct wave number. Function $f(z)$ is a Taylor expansion of free surface over the depth:

$$f(z) = f(\eta) + \frac{df(\eta)}{dz}(z - \eta) + \frac{1}{2} \frac{d^2 f(\eta)}{dz^2}(z - \eta)^2 + \frac{1}{6} \frac{d^3 f(\eta)}{dz^3}(z - \eta)^3 + \frac{1}{24} \frac{d^4 f(\eta)}{dz^4}(z - \eta)^4 + O((z - \eta)^5). \quad (17)$$

If the absolute error is set to a constant E for every vertical location and the function $f(z)$ and its derivatives are known, one can find a maximum cell size $\Delta z(\eta) = z - \eta$ at every location (Pakozdi et al., 2021):

$$E(z, \eta) = f(z) - \left(f(\eta) + \frac{df(\eta)}{dz}(z - \eta) + \frac{1}{2} \frac{d^2 f(\eta)}{dz^2}(z - \eta)^2 \right), \quad (18)$$

$$0 = E - f(\eta + \Delta z) + \left(f(\eta) + \frac{df(\eta)}{dz}(z - \eta) + \frac{1}{2} \frac{d^2 f(\eta)}{dz^2}(z - \eta)^2 \right). \quad (19)$$

2.3. Wave generation, dissipation and breaking

Flexible wave generation methods are implemented in the REEF3D framework (Bihs et al., 2016). When a relaxation method (Larsen and Dancy, 1983; Mayer et al., 1998) is used for the wave generation, the relaxation function is formulated as the following:

$$\Gamma(\tilde{x}) = 1 - \frac{e^{(\tilde{x}^{3.5})} - 1}{e - 1} \quad \text{for } \tilde{x} \in [0; 1], \quad (20)$$

where \tilde{x} is scaled to the length of the relaxation zone. The free surface velocity potential $\tilde{\phi}$ and the surface elevation η are increased to the analytical values in the wave generation zone:

$$\Theta(\tilde{x})_{relaxed} = \Gamma(\tilde{x})\Theta_{analytical} + (1 - \Gamma(\tilde{x}))\Theta_{computational}. \quad (21)$$

Following the same methodology, the free surface velocities potential $\tilde{\phi}$ and the surface elevation η are reduced to zero or initial still water values in the wave energy dissipation zone or numerical beach to eliminate wave reflection of the outlet boundaries.

Waves can also be generated at the inlet using a Neumann boundary condition where the spatial derivatives of the velocity potential are defined. In this way, the velocity potential at the boundary is calculated using the desired analytical horizontal velocity:

$$\varphi_{i-1} = -u(\mathbf{x}, z, t) \Delta x + \varphi_i, \quad (22)$$

where $u(\mathbf{x}, z, t)$ is the analytical horizontal velocity.

In addition, wavemaker motion input can also be used to generate waves in the numerical wave tank (NWT). In the current model, three types of wavemaker motions can be used: piston-type wavemaker, flap-type wavemaker and double-hinged flat-type wavemaker. This enables the numerical model to reproduce most of the experimental wave measurements for both shallow and deepwater.

In the presented potential flow model, the free surface is represented by a single value, therefore it is not possible for the model to represent an over-turning breaker as in a CFD simulation (Bihs et al., 2016). However, correct detection of wave breaking events and energy dissipation can be achieved with a breaking wave algorithm. The proposed model aims to address both steepness-induced deepwater wave breaking and depth-induced shallow water breaking.

The depth-induced wave breaking is activated when the vertical velocity of the free-surface exceeds a fraction of the shallow water celerity (Smit et al., 2013; Zijlema et al., 2011):

$$\frac{\partial \eta}{\partial t} \geq \alpha_s \sqrt{gh}. \quad (23)$$

$\alpha_s = 0.6$ is recommended from the test of Smit et al. (2013), which also agrees with a similar study performed by Lynett (2006).

Deepwater steepness-induced breaking is activated with a steepness criterion:

$$\frac{\partial \eta}{\partial x_i} \geq \beta, \quad (24)$$

where $\beta = 0.3$ is recommended by Smit et al. (2013) from the comparison to physical tests.

After a wave breaking is detected, two methods are available to represent the energy dissipation during the wave breaking process. The first method is a geometric filtering algorithm that smoothens the free surface for energy dissipation (Jensen et al., 1999). Here, an explicit scheme is used and therefore there is no CFL constraint. Another method is to introduce a viscous damping term in the free surface boundary conditions locally around the breaking region (Baquet et al., 2017). When wave breaking is detected, the free surface boundary conditions Eqs. (2) and (3) then become:

$$\frac{\partial \eta}{\partial t} = -\frac{\partial \eta}{\partial x} \frac{\partial \tilde{\phi}}{\partial x} - \frac{\partial \eta}{\partial y} \frac{\partial \tilde{\phi}}{\partial y} + \tilde{\omega} \left(1 + \left(\frac{\partial \eta}{\partial x} \right)^2 + \left(\frac{\partial \eta}{\partial y} \right)^2 \right) + \nu_b \left(\frac{\partial^2 \eta}{\partial x^2} + \frac{\partial^2 \eta}{\partial y^2} \right), \quad (25)$$

$$\frac{\partial \tilde{\phi}}{\partial t} = -\frac{1}{2} \left(\left(\frac{\partial \tilde{\phi}}{\partial x} \right)^2 + \left(\frac{\partial \tilde{\phi}}{\partial y} \right)^2 \right) - \tilde{\omega}^2 \left(1 + \left(\frac{\partial \eta}{\partial x} \right)^2 + \left(\frac{\partial \eta}{\partial y} \right)^2 \right) - g\eta + \nu_b \left(\frac{\partial^2 \phi}{\partial x^2} + \frac{\partial^2 \phi}{\partial y^2} \right), \quad (26)$$

where ν_b (m^2/s) is the artificial turbulence viscosity. ν_b is calibrated from the comparison of the potential flow model simulations with model test data and the CFD simulations. As a result, the value of ν_b is recommended to be 1.86 (Baquet et al., 2017) for the offshore deepwater conditions and 0.0055 for shallow water breaking in the proposed model. In the new free surface boundary conditions Eqs. (25) and (26), the newly introduced diffusion term is treated with an implicit time scheme so that there is no extra constraint on time step sizes.

The two wave breaking methods can also be used combined for challenging wave breaking scenarios. Wave breaking is detected whenever one of the detection criteria is fulfilled, either when wave steepness exceeds a threshold, or vertical velocity exceeds a threshold. Therefore, the process is automatic. In some cases, both energy dissipation methods can be used at the same time for sufficient energy dissipation in extreme sea states. In this case, the artificial viscosity is added in the free surface boundary conditions, while the filtering algorithm smoothens the free surface geometrically.

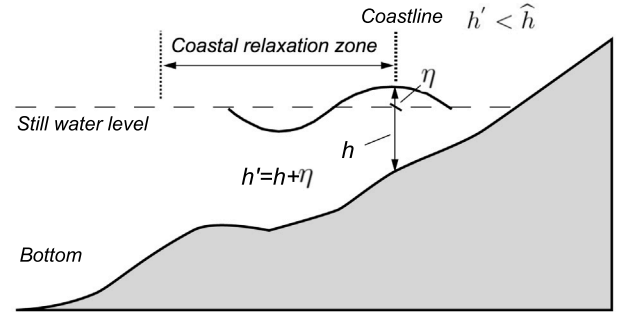


Fig. 1. Illustration of the still water level h , local water depth h' , free surface elevation η and coastline detection algorithm.

2.4. Coastline detection and treatment

Handling the complex coastline has been a challenge when applying a potential flow model in the coastal area. The first difficulty is efficient grid generation around the complex boundaries. The structured curvilinear grid presented in OceanWave3D (Engsig-Karup et al., 2009, 2012; Glimberg et al., 2013) provides one solution. However, it might be challenging to approximate the coastline geometry with a structured curvilinear grid around complex and sharp curves. The accuracy of the coastline is also sensitive to the grid resolution at the coastline. The second difficulty is possible numerical instability during the wave run-up process in the swash zone. The vertical velocity in the free surface boundary condition Eq. (7) cannot be given directly but calculated from derivatives of velocity potential over water depth. In some scenarios, there is a thin layer of water in the swash zone where the water depth can be considered as infinitesimal. In such cases, the vertical derivative of the velocity potential at the free surface tends to be ill-defined. This tends to cause unreasonably high particle velocities at certain regions along the coast. When the focus is large-scale modelling where the swash zone dynamics has less influence on the wave propagation in the rest of the domain, the swash zone dynamics can be treated with a simpler boundary condition. Under this assumption, an efficient and flexible coastline algorithm is introduced to address these two difficulties.

First, the computational cells are identified as wet cells and dry cells following a relative-depth criterion. The local water depth h' is defined as a sum of still water level h and the free surface elevation η :

$$h' = \eta + h. \quad (27)$$

η is the surface elevation, h is the still water level measured from the bottom. The relationship among h' , h and η is illustrated in Fig. 1.

If the local water depth h' is smaller than a threshold \hat{h} , then the local cell is identified as a dry cell. When a cell is identified as a dry cell, the velocities in the cell is set to be zero:

$$\begin{cases} u = 0, & \text{if } h' < \hat{h}, \\ v = 0, & \text{if } h' < \hat{h}. \end{cases} \quad (28)$$

The default threshold is set to be 0.00005 m according to the practice of Zijlema et al. (2011), however, it can be customised based on the specific conditions. The approach tracks the variation of the shoreline accurately and avoids numerical instabilities by ensuring non-negative water depth (Stelling and Duinmeijer, 2003; Zijlema and Stelling, 2008).

After the wet and dry cells are identified, the wet cells are assigned with a value +1 and the dry cells are assigned with a value -1. With the signed initial values, the coastline is captured using a level-set function (Osher and Sethian, 1988):

$$\phi_{ls}(\vec{x}, t) \begin{cases} > 0 \text{ if } \vec{x} \in \text{wet cell}, \\ = 0 \text{ if } \vec{x} \in \Gamma, \\ < 0 \text{ if } \vec{x} \in \text{dry cell}. \end{cases} \quad (29)$$

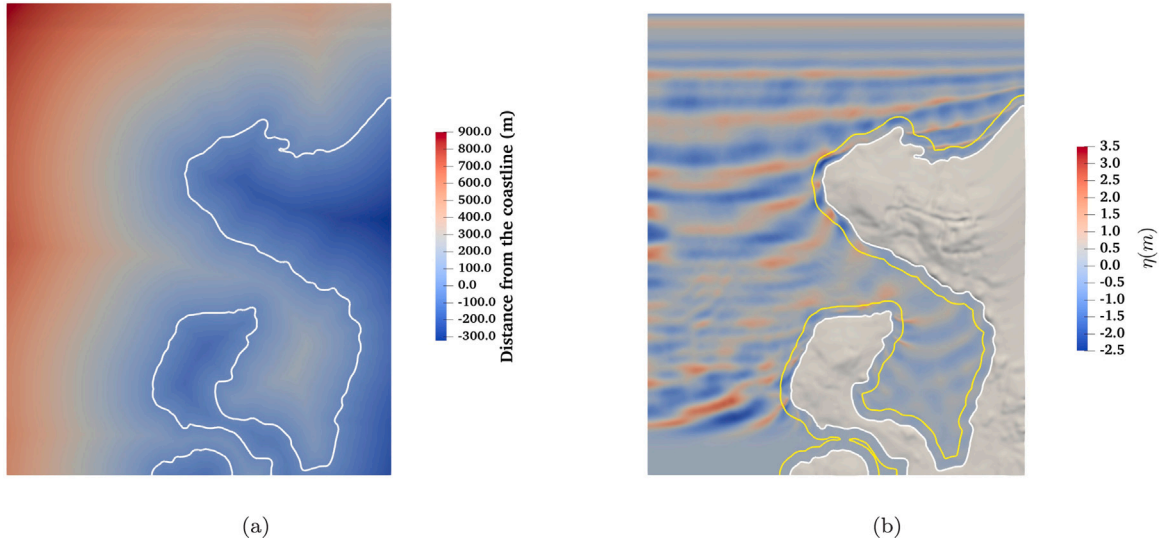


Fig. 2. Detection of the coastline and calculation of distance from the coastline for a complicated topography using the proposed coastline algorithm. The white contour in (a) is the detected coastline, the colour shows the distance away from the coastline, with negative values indicating inland and positive values indicated offshore. The yellow contour in (b) is the boundary of the coast-following relaxation zone to reduce numerical instability and customise reflection properties of the coastline.

Γ indicates the coastline, and the Eikonal equation $|\nabla\phi_{ls}| = 1$ holds valid for the level-set function. The distance perpendicular to the coastline is also calculated based on the level-set method. From the initial values, the correct signed distance function is obtained by solving the following Partial Differential Equation (PDE) based reinitialisation function (Sussman et al., 1994). This equation is solved until convergence and results in the correct signed distance away from the coastline in the whole computational domain. The exact coastline location is the zero-contour of the level set function.

$$\frac{\partial\phi_{ls}}{\partial t} + S(\phi_{ls}) \left(\left| \frac{\partial\phi_{ls}}{\partial x_j} \right| - 1 \right) = 0, \quad (30)$$

where $S(\phi_{ls})$ is the smoothed sign function (Peng et al., 1999).

Relaxation zones are applied along the wet side of the coastline covering a given distance from the coastline. The size of the coast zone is usually small in order to preserve the correct coastline geometry and minimise the influence on flow conditions. An additional breaking wave viscosity ν_b is added to the free surface boundary conditions. The relaxation function ramps down the velocity potential and the free surface elevation to zero and ramps up additional viscosity from the outer boundaries of the coast zone to the coastlines to further dissipate wave energy. This gradual process is described in Eq. (31), which can be generally considered as a reverse process of the wave generation zone as shown in Eq. (21). It is considered sufficiently accurate for engineering purposes as noted by Engsig-Karup et al. (2013). The breaking wave algorithms are also active in case of wave breaking within the coastal zone. The effects from the relaxation function, the added viscosity and breaking algorithms work together to effectively dissipate wave energy within a narrow coast zone. As a result, the coastal relaxation zone help to avoid extreme run-ups in the swash zone and eliminate numerical instabilities in the free surface boundary conditions in extreme shallow regions. In addition, the reflection property of the coastline can be customised by adjusting the strength or size of the coastal relaxation zones.

$$\begin{aligned} \phi(\tilde{x}) &= (1 - \Gamma(\tilde{x})) \phi(x, y), \\ \eta(\tilde{x}) &= (1 - \Gamma(\tilde{x})) \eta(x, y), \\ \nu_b(\tilde{x}) &= \Gamma(\tilde{x})\nu_{b0}, \end{aligned} \quad (31)$$

where $\phi(x, y)$, $\eta(x, y)$ and ν_{b0} are the velocity potential, the free surface elevation and the added breaking wave viscosity at the outer boundaries of the coast zones. $\Gamma(\tilde{x})$ is the relaxation function as shown in Eq. (20).

The proposed coastline algorithm (see Fig. 2) is intended to have the following beneficial features:

(1) The level-set approach is flexible and universal. The convergence of the horizontal grid is associated with the characteristic wavelength. As a result, the resolution of the coastline geometry captured by the level-set method represents the relevant coastal features for the input waves. There is no need for coastline-following (i.e. body-fitted) grid generation. Therefore, the algorithm is less case-dependent.

(2) The level-set method enables accurate capture of the shoreline positions in an implicit manner. The method uses a smooth signed distance function for the coastline geometry rather than representing the coastline geometry with a body-fitted grid. This is in contrast to structured curvilinear grid or multi-block approach (Engsig-Karup et al., 2009, 2012; Glimberg et al., 2013).

(3) As a result of the first two features, the proposed method ensures the quality of the grid in the horizontal plane and facilitates the implementation of high-order discretisation schemes for the free surface boundary conditions for the representation of complex nonlinear phenomena. With the structured horizontal grid, domain decomposition and parallel computation are also made straightforward.

(4) The coastal relaxation zones eliminate possible instabilities in infinitesimal thin water layers. The impact on the large-scale wave propagation from the coastal zone can also be minimised from sensitivity studies.

As a result, the algorithm is expected to include various complex coastlines with a straightforward, efficient and consistent grid generation. The coastal relaxation zones do not resolve the detailed swash zone dynamics and thus might not be suitable for all numerical models and applications where the validation against those physical processes is more important. However, they facilitate stable large-scale wave propagation simulations in the proposed numerical framework.

3. Numerical simulations of wave propagation

In this section, the numerical wave model is validated against theory and experimental measurements to demonstrate its flexibility and accuracy for different scenarios. A 5th-order Stokes wave propagation over a constant water depth is simulated for over 160 wave periods to show the accurate representation of the free surface after long-duration wave propagation. Wave propagation over a submerged bar in intermediate water depth is simulated to demonstrate that both shoaling and de-shoaling processes are well reproduced in the proposed

numerical model. A simulation of wave propagation over a steep slope from deep to shallow water is performed to prove that the model is able to represent wave transformation over significant wave depth variation within a short horizontal distance. And finally, the breaking algorithm is proven to be effective for a wave breaking over a mild slope.

3.1. Steep nonlinear wave propagation in deepwater

A steep 5th-order Stokes wave (Fenton, 1985) is generated and propagated in a 2D numerical wave tank for a distance of 40 wavelengths in constant deepwater with $kh = 2\pi$. The input wave height is 0.1275 m and the wavelength is 1 m. This results in a wave steepness of $H/L = 0.1275 = 90\%(H/L)_{\text{breaking}}$, which is the deepwater breaking limit (Le Méhauté, 1976). The waves are generated following the algorithm of Clamond and Dutykh (2018) in a wave generation zone with a relaxation function. The wave generation zone is five wavelengths long to achieve stable wave propagation for such a nonlinear and steep wave. This is in contrast to the one-wavelength generation zone configuration for mildly nonlinear waves, as reported in Bihs et al. (2020). Correspondingly, a 10-wavelength numerical beach is arranged at the outlet boundary of the numerical wave tank to eliminate wave reflection. A constant water depth of one wavelength is used throughout the entire domain. This steep nonlinear wave is simulated for 120 s, corresponding to over 160 wave periods. Ten cells with a stretching factor of 2.45 are used in the vertical direction. Adaptive time-stepping is used in all simulations where the CFL number is 0.5. Though $CFL = 1.0$ is normally sufficient for the simulation of most wave propagations (Bihs et al., 2020), a smaller time step is used here to ensure a stable shape of the near-breaking steep wave. The grid convergence study is performed by evaluating the wave surface elevations in time and space, the correlation coefficient between the simulated waves and theoretical calculations from Fenton (1985) and mass and energy conservation. The grid convergence investigations are summarised and presented in Fig. 3.

The grid convergence study is performed with the optimal vertical grid choice. In order to demonstrate the effect of the vertical grid arrangement, the surface elevations are compared when using different vertical stretching factors, as shown in Fig. 4. It is seen that a stronger vertical stretching factor α leads to a higher celerity and a higher wave crest, while a smaller α results in the opposite effects. The optimal choice following the constant truncation error method gives the best results both for the wave celerity and amplitude. The relative wave number error using different stretching factors are also compared in Fig. 4c. It confirms that the optimal vertical stretching factor yields a minimal wave number error.

From Figs. 3a and 3b, it is seen that the free surface elevations match the theoretical wave amplitudes and wave phases when the cell size is reduced to 0.02 m or smaller. The estimated wave heights also tend to converge towards the theoretical input wave height with 0.02 m or smaller horizontal cell sizes, as seen in Fig. 3c. Furthermore, the correlation relation between the simulated surface elevation in space and the theoretical calculation is plotted over the simulation time in Fig. 3c. The simulated waves reach a static status after nearly 50 s propagation. Afterwards, a near-constant correction coefficient around 1.0 is found with both 0.01 m and 0.02 m cell sizes. This confirms that the simulated free surface is in synchronisation with the theoretical calculations and that the wave celerity is well represented. Figs. 3a to 3d demonstrate that the wave free surface is well represented in the presented numerical wave tank over the duration of the simulation and a good agreement is achieved when comparing with the theory. Furthermore, the conservation of mass or volume and total energy (the sum of kinematic and potential energy) are examined in Figs. 3e and 3f. It is seen that the error of the volume of the fluid domain is nearly constant over the duration of the simulation when a cell size of 0.02 m or smaller is used. Small fluctuations within $\pm 0.25\%$ is observed possibly due to the integration errors of fluid properties in the water column. A

stable small fluctuation with an amplitude of 0.15% around a constant mean offset of 0.35% is observed when a static status is achieved after 50 s with the fine grids. For both errors, larger cell sizes produce more significant fluctuations. Therefore, it is concluded that a cell size of 0.02 m is sufficient for a good representation of the chosen wave.

With the chosen cell size and the chosen vertical grid arrangement, the free surface elevations obtained in the NWT using different spatial discretisation schemes for the free surface boundary conditions are compared in Fig. 5. 2nd-, 4th- and 6th-order central differencing schemes (CDS) and 3rd- and 5th-order WENO schemes are used in the comparison. It is seen that central differencing schemes fail to keep the stable shape of the propagating waves even with up to 6th-order accuracy. WENO schemes are able to capture the sharp waveforms in a more accurate and stable manner. The 5th-order WENO scheme shows an increased accuracy over the lower order counterpart. The comparison provided motivation for the choice of high-order WENO schemes for an accurate representation of surface waves, especially for steep and nonlinear waves.

It is seen that, with the chosen cell size and the numerical setup, the proposed model is able to accurately represent the long duration stable propagation of a transient steep regular wave with a wave steepness corresponding to 90% deepwater breaking limit.

3.2. Wave propagation over a submerged bar

One of the challenges in a shallow-water model is the de-shoaling process (Wang et al., 2020b), where a single frequency wave decomposes into higher frequency short wave components after propagating over a shallow water region. Those high-frequency components are usually so short that shallow water assumptions are not valid any longer. This leads to significant errors in both wave amplitude and phase. Therefore, the monochromatic long wave propagation over a submerged bar experiment performed by Beji and Battjes (Beji and Battjes, 1993) is simulated to show the presented model's ability to represent the de-shoaling process. The configuration of the numerical wave tank is shown in Fig. 6. A 2nd-order Stokes wave with a wave height $H = 0.021$ m and a wave period $T = 2.525$ s is generated in a relaxation zone at the inlet of the numerical wave tank. The wave generation zone is 5 m long, covering slightly more than one wavelength. A submerged bar is located 6 m from the end of the wave generation zone. Eight wave gauges are located at $x = 11, 16, 17, 18, 19, 20, 21, 22$ and 24 m over the submerged bar, as shown in Fig. 6. A relaxation zone of two wavelengths for wave dissipation is arranged at the outlet of the numerical wave tank. All simulations are performed for 60 s. Adaptive time-stepping is used while $CFL = 1.0$ is maintained. 10 vertical cells with a stretching factor α of 3.0 are used following the constant-truncation-error method. Four cell sizes are used for the grid convergence study: $dx = 0.02$ m, 0.04 m, 0.08 m and 0.16 m. The de-shoaling process is most prominent at wave gauge 8. Therefore, the time series of surface elevation at the wave gauge 8 obtained using different cell sizes are compared in Fig. 7a and the frequency spectra derived from these time series are compared in Fig. 7b. It is seen that both $dx = 0.02$ m and 0.04 m reproduce the experimental wave amplitude and frequency spectrum very well. However, there is a slightly larger phase error in the simulation with $dx = 0.04$ m in comparison to $dx = 0.02$ m. Therefore, $dx = 0.02$ m is used in the following validation against the experiment.

The σ -grid with $dx = 0.02$ m is visualised in Fig. 8 at $t = 60$ s. Here, the horizontal grid is equal-distant and the vertical grid is denser closer to the free surface. In addition, the vertical grid follows the variation of the bottom topography as well as the surface elevation.

Moreover, the horizontal velocity field at $t = 60$ s is shown in Fig. 9. The velocities are highest at the free surface and decrease over depth, the vertical velocity distribution is faithfully represented in the presented simulation.

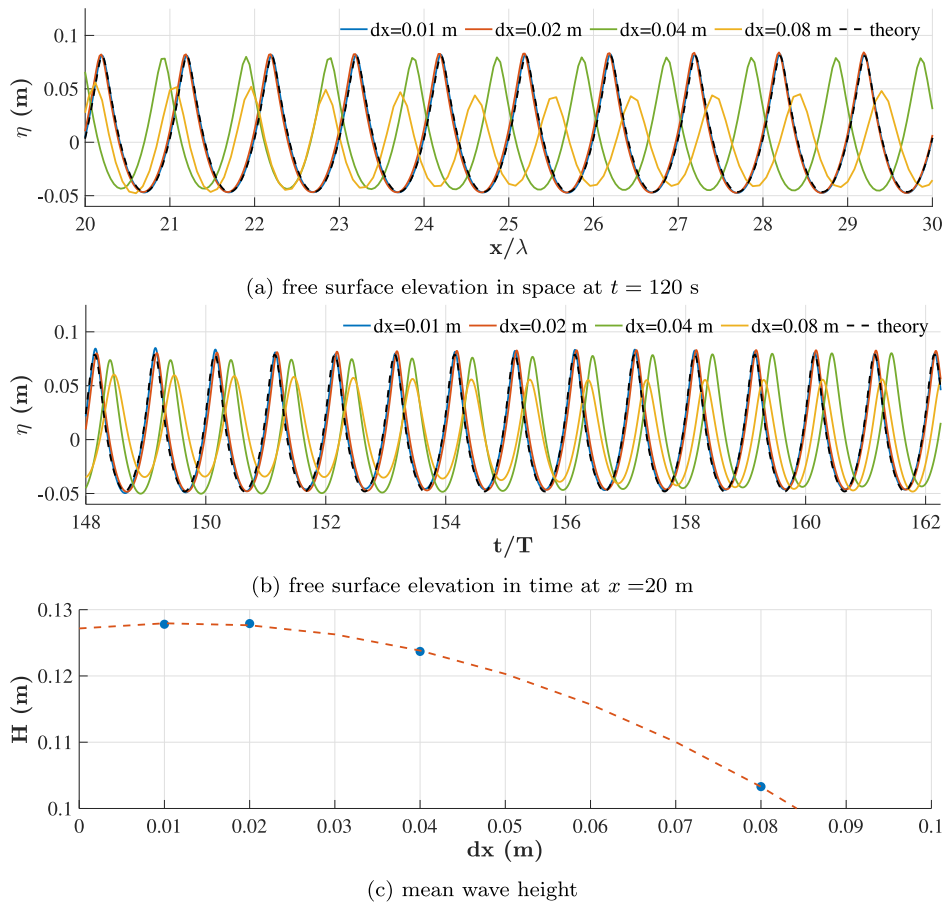


Fig. 3a. Grid convergence investigation of steep nonlinear wave propagation in deepwater where $H/H_{max} = 0.9$ (part 1).

Both the time series and the frequency spectra at all wave gauges are compared in 10 between the experimental measurements and numerical simulations.

From gauge 1 to 3, wave shoaling takes place, the wave height increases and higher frequency components start to appear. The wave crests, troughs and the emerging high-frequency components in the numerical simulations all agree well with the experiments. While the wave propagates over the shallow water region at the height of the submerged bar, even higher frequency components appear, and the wave energy starts to shift from low-frequency components to high-frequency components. During the process, up to six notable frequencies are observed and the highest frequency is near 2.5 Hz. The simulated wave in the numerical wave tank represents all six frequencies as in the experiments, the energy distribution among the six frequencies are also correctly represented. When the waves pass wave gauges 6, 7 and 8, the de-shoaling process becomes more significant. Here the wave energy from high-frequency components overtakes the original input wave frequency. With only four major frequency components left, more than half of the wave energy is shifted to the frequency range higher than 1 Hz. During the entire wave transformation process, the numerically simulated wave crests, troughs, phases and wave profiles are close to the experimental measurements. The number of frequency components and energy distribution over the frequencies in the numerical wave tank also agree with the experiment. The model simulates the wave transformation over a submerged bar with good agreement, including high-frequency details.

3.3. Bi-chromatic wave propagation over a steep ramp

Steep slopes over 45° are typical near the Norwegian coast and challenging for numerical modelling. The grid needs to undergo severe distortion following step-like topography changes. In this section,

wave propagation over a steep slope from deepwater to shallow water conditions is simulated. The NWT configuration follows the experiment conducted at SINTEF Ocean in Trondheim (Pákozdi et al., 2019). The illustration of the NWT setup is shown in Fig. 11. The steep slope consists of two segments, the first segment starts 2.1 m from the wavemaker and has a slope of 70° , the second segment has a slope of 45° . The water depth is 10 m at the wave generator and 0.75 m after the slope. A double-hinged flap wavemaker is used for the wave generation of a bi-chromatic wave train. In order to reproduce the same waves as in the experiment, the wavemaker motion in the physical test is used to drive the waves in the NWT instead of the relaxation method. A relaxation zone of 9.5 m is located at the outlet of the numerical wave tank to absorb wave energy and eliminate reflection. Wave gauge G0 is located at $x = 1$ m in the deepwater region before the slope, wave gauges 1–3 are located at $x = 10$, 35 and 50 m in the shallow water region after the slope. 15 cells and a stretching factor of 3.0 are used in the vertical direction following the constant-truncation-error method described in Section 2.2. For the time step size, $CFL = 1.0$ is kept constant. Three cell sizes are used for the grid convergence study: $dx = 0.05$ m, 0.10 m and 0.20 m. All simulations are performed for 180 s. The time series and frequency spectra at wave gauge 0 obtained using different cell sizes are compared in Fig. 12. Both $dx = 0.05$ m and 0.10 m represent the two frequencies and the corresponding spectra energy density accurately, however, the wave phase is better represented with the cell size $dx = 0.05$ m. Therefore, $dx = 0.05$ m is used in the following analysis in this section.

With the chosen grid resolution, the grid at the steep ramp is shown in Fig. 13. In spite of the significant bathymetry change, the σ -grid follows the topography very well.

The surface elevation time histories obtained from the numerical simulations are then compared with the experimental measurements

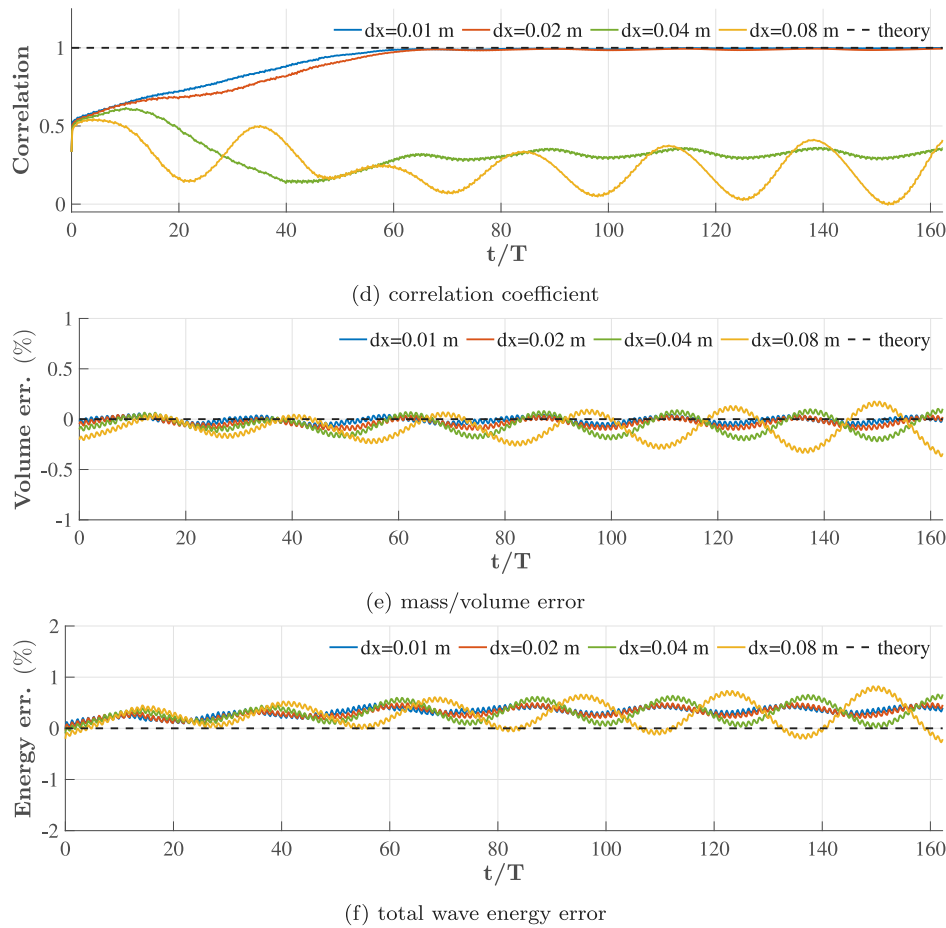


Fig. 3b. Grid convergence investigation of steep nonlinear wave propagation in deepwater where $H/H_{max} = 0.9$ (part 2). (a) free surface elevation in space at $t = 120$ s ($t/T = 162.5$, T is wave period), (b) free surface elevation in time at $x = 20$ m ($x/\lambda = 20$), (c) mean wave height in the numerical wave tank at $t = 120$ s ($t/T = 162.5$), (d) correlation coefficient between the simulated surface elevation and theoretical values estimated using the method by Fenton (1985), (e) mass/volume error over time, (f) total wave energy error over time.

in Fig. 14. The input wave signal of the bi-chromatic wave is seen in Fig. 14a, and the simulated free surface time series at the wave gauges G1 to G3 show an accurate representation of the experimental wave profiles, amplitudes and wave phases.

As the bi-chromatic wave propagates over the steep ramp, additional second-order wave components at sum- and difference-frequencies appear as a result. It is found in Fig. 12b that the two principal frequencies of the bi-chromatic wave are $\omega_1 = 0.54$ Hz and $\omega_2 = 0.74$ Hz. In theory, four new bounded frequencies should appear: $\omega_3 = \omega_2 - \omega_1 = 0.2$ Hz; $\omega_4 = 2\omega_1 = 1.08$ Hz; $\omega_5 = 2\omega_2 = 1.48$ Hz and $\omega_6 = \omega_1 + \omega_2 = 1.28$ Hz. The time series at wave gauge 2 from the numerical simulation and experimental measurements are used to calculate the frequency spectra. The resulting spectra are compared in Fig. 15 for each of the frequency components.

It is seen that all theoretical frequency components are represented in the frequency spectra from both the experiment and the simulations. The simulation captures the two principal frequencies ω_1 and ω_2 and the low-frequency ω_3 exactly as the theoretical values and the corresponding energy densities are nearly identical to the experiment. The high frequencies represented in the numerical simulation are slightly different from the experiment, and the relevant energy densities show a difference of 10 – 25%. However, the energy densities at the high-frequency range are very small (10^{-5} to 10^{-4}) in comparison to the principal frequencies (10^{-2}). The energy differences between the simulation and the experiment at the high-frequency range is negligible when they are compared in the same scale as the principal frequencies.

3.4. Wave breaking over a mild slope

In shallow water regions close to the shoreline, depth-induced wave breaking is a common phenomenon. However, depth-induced wave breaking is not included in most potential flow models as their focus is mostly on deepwater. In the presented model, a consistent wave breaking algorithm over a complete range of water depths is introduced. In this section, a depth-induced plunging wave breaker near the coastline over a mild-slope (Ting and Kirby, 1995) is simulated. The numerical wave tank setup is shown in Fig. 16. The slope starts 5.8 m from the wave generation boundary and rises up to 0.748 m at the outlet following a slope of 1:35. The water depth at the wave generator is 0.4 m. A 5th-order cnoidal wave with a wave height of 0.128 m and wave period of 5 s is generated at the inlet using Neumann boundary conditions. Here, the Neumann boundary condition is a more efficient method for wave generation as the analytical description of the cnoidal wave velocity potential is more complicated. Four wave gauges are located on the slope adjacent to the wave breaking location. From wave gauges 1 to 4, the x-coordinates are $x = 11.8, 12.8, 13.8$ and 14.1 m. The artificial viscous damping factor of 0.0055 is used in the following simulation for the correct representation of wave energy dissipation during the wave breaking process. 10 vertical cells are used following the constant-truncation-error method described in Section 2.2 based on the water depth before the slope. The simulations are performed for 40 s with adaptive time stepping and a constant $CFL = 1.0$. Three cell sizes are used in the grid convergence study $dx = 0.05$ m, 0.10 m and 0.20 m. The time histories of water surface elevation at the wave gauges

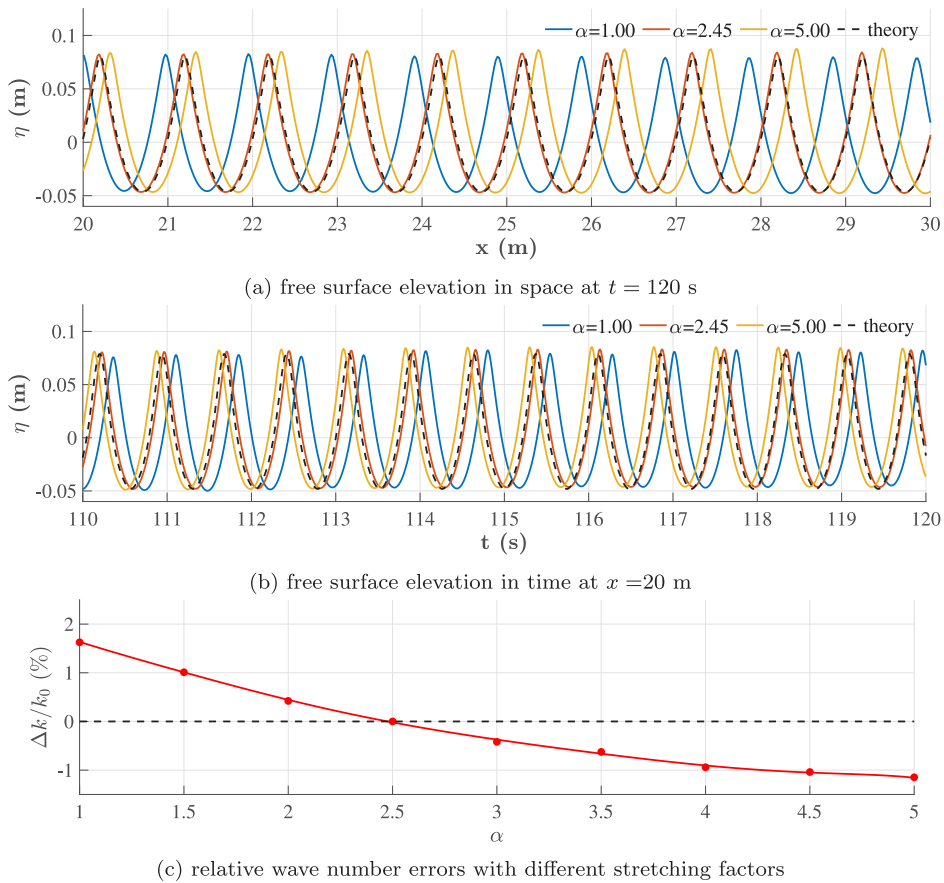


Fig. 4. Effects of the vertical grid choice in the simulations of the steep nonlinear wave propagation. (a) and (b) show the free surface elevations in space and time using a uniform grid ($\alpha = 1.0$), the optimal stretching from the constant truncation error method ($\alpha = 2.45$) and a strong stretching ($\alpha = 5.0$). (c) the relative wave number error defined by the absolute wave number differences Δk divided by the theoretical wave number k_0 .

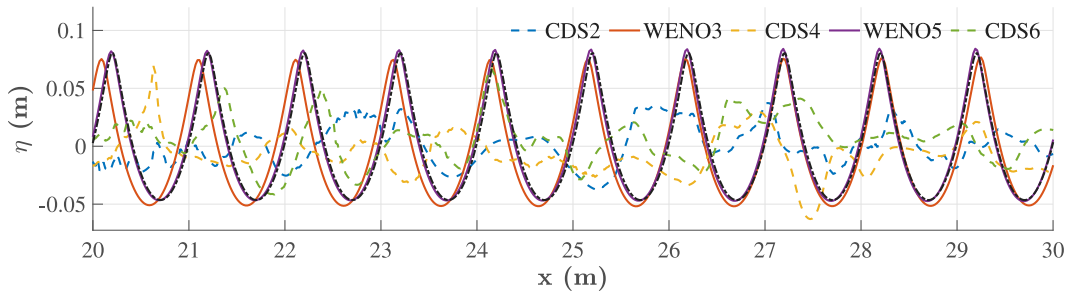


Fig. 5. Free surface elevations obtained from simulations using different spatial discretisation schemes for the free surface boundary conditions. CDS2, 4 and 6 represent 2nd-, 4th- and 6th-order central differencing schemes, WENO3 and 5 represent 3rd- and 5th-order WENO schemes. The black dash-dotted line represents the theory.

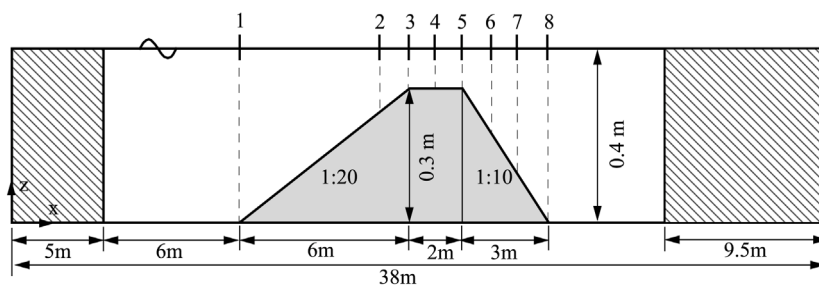


Fig. 6. Numerical wave tank setup for the wave propagation over a submerged bar.

2 and 3 obtained from the numerical wave tank with different cell sizes are compared in Fig. 17.

As can be seen from Fig. 17, $dx = 0.05$ m provides a good representation of the wave crest, the wave profile as well as the phase information,

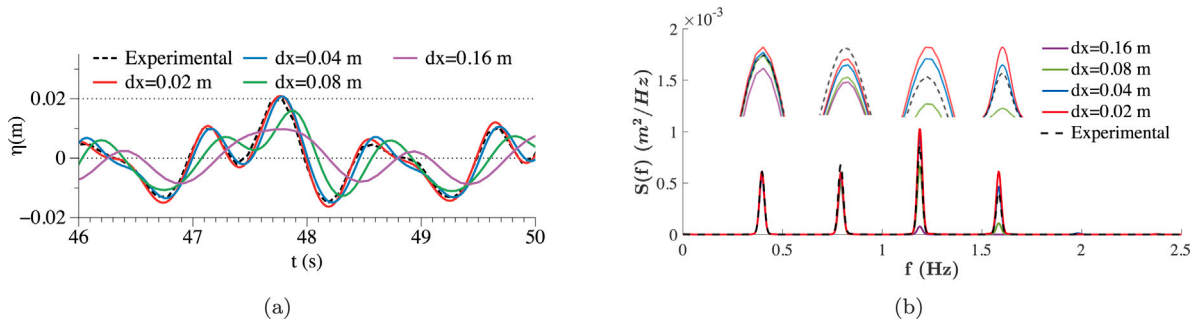


Fig. 7. Grid convergence for the simulation of a 2nd Stokes wave propagating over a submerged bar. The amplified zoom-in view of each spectrum peak are illustrated above each harmonics for clarity.

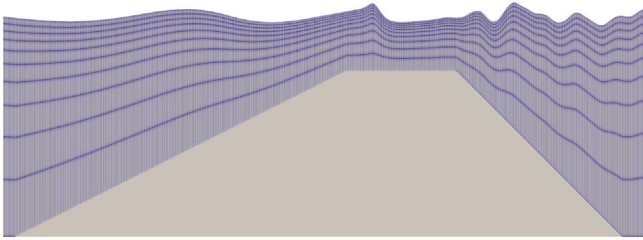


Fig. 8. σ -grid with $dx = 0.02$ m at $t = 60$ s in the simulation of wave propagation over a submerged bar (only the grid near the submerged bar is shown). 10 cells and a stretching factor of 3.0 are used in the vertical direction. The grid is amplified by a factor of 5 in the vertical direction for visualisation purposes.

while coarser grids show a constant underestimation of the wave crest. With the chosen grid configuration, the coastal zone width convergence study is performed with four difference widths 1 dx , 2 dx , 3 dx and 4 dx , where dx is the horizontal cell size. The simulated time series at wave gauges 2 and 4 using the different coastal zones are compared in Fig. 18. It is seen that the unrealistic wave run-up and run-down in the swash zone with near infinitesimal water depth results in spurious waves near 30 s when only one cell is used for the coastal zone. With a wider coastal zone, the simulation results are very similar to each other. As a result, 2 dx is chosen for the simulation since it is the minimum width that gives consistent results while eliminating the swash zone instabilities. Similarly, the sensitivity study on the choice of the viscous damping factor ν_b in the breaking algorithm is demonstrated in Fig. 19. It is seen that a stronger ν_b leads to too much energy dissipation, $\nu_b = 0.0055$ gives a good representation of the wave crest changes after wave breaking. Therefore, it is also recommended to calibrate the wave breaking parameters with a benchmark before further studies.

Using $dx = 0.05$ m, 2 cells at the coastal zone and $\nu_b = 0.0055$, the time series of surface elevation at all four wave gauges are compared with the experiment in Fig. 20. It is observed that the wave crest increases from wave gauge 1 to wave gauge 2, showing a strong shoaling. Then the wave crest has a sudden decrease at wave gauge 3, indicating that wave breaking occurs between wave gauges 2 and 3. The relative errors ϵ of the wave crest heights are also shown in Fig. 20 besides each wave crest. The relative errors are found to be lower than 5% in general, except for the second peak in Fig. 20b. The simulated wave crests follow the experiment well both before and after the breaking, showing the correct energy dissipation in the implemented breaking algorithm. The coastal relaxation zones help to represent the characteristics of the experimental flow field and ensure the correct breaking wave location, indicating a close representation of the reflection and dissipation properties of the coastline, though the details of the run-up and run-down processes are not resolved.

One of the wave breaking events is shown in Fig. 21. Here, the wave crest increase to its maximum and the wave front becomes vertical. Since the free surface is single-valued, a visualisation of overturning

breaker is not within the scope of the model. However, it is seen from Fig. 20 and Fig. 21 that the breaking event is correctly detected and the wave energy is correctly dissipated in the numerical simulation.

3.5. Wave shoaling over a three-dimensional submerged reef

The previous sections demonstrate the effectiveness and accuracy of the proposed numerical model for 2D wave propagation and transformation. In this section, a 3D wave shoaling over a semi-circular submerged reef is investigated. The numerical setup follows the experimental configuration reported by Whalin (1971). The schematics of the numerical wave tank is illustrated in Fig. 22. The numerical domain is 35 m long and 6.096 m wide with a constant water depth of 0.457 m at the wave generation zone and 0.1524 m over the top of the reef at the numerical beach. At the centreline of the numerical wave tank ($y = 3.048$ m), the semi-circular submerged reef starts from $x = 7.62$ m with a slope of 1 : 25 until $x = 15.85$ m where the reef reaches its maximum height of 0.3046 m. Nineteen wave gauges are arranged along the centreline between $x = 3.505$ m and $x = 11.731$ m with a constant interval of 0.457 m in between two wave gauges. Thereafter, another 20 wave gauges are arranged between $x = 13.868$ m and $x = 22.551$ m with the same constant interval 0.457 m. A 2nd-order Stokes wave with a wave height $H = 0.015$ m and a wave period $T = 2$ s is generated at the wave generation zone of one wavelength. A numerical beach of two wavelengths is arranged at the outlet boundary to eliminate wave reflection.

Fifty wave periods (100 s) are simulated to obtain statistical properties of the various harmonics from the shoaling process. The wave harmonics are identified using a Fast Fourier Transform (FFT) method from the simulated time series at each waves gauge. After a grid convergence study on each of the harmonics, a cell size of 0.05 m is found to be sufficient for numerically converged results. A similar grid resolution is also reported in a previous study on the same case as reported by Engsig-Karup et al. (2009). Ten vertical cells with a stretching factor of 1.0 (uniformly distributed) are used in the simulation. The simulated surface elevation at the last time step $t = 100$ s is shown in Fig. 23. The shoaling waves around the semi-circular reef converge at the top of the reef, creating higher waves and introducing significant non-linear effects. In order to validate the model for representing this nonlinear process, the different harmonics in the simulated wavefield using REEF3D:FNP are compared with the experimental measurements recorded by Whalin (1971) and the numerical simulation results from the fully nonlinear potential flow model OceanWave3D (Engsig-Karup et al., 2009). The comparison is shown in Fig. 24.

Fig. 24 shows that the amplitudes of the first three harmonics follow similar spatial variations along the centreline as the experiment as well as the OceanWave3D simulations. It can be concluded that the model is able to represent nonlinear 3D wave transformations with good accuracy when compared with experiments and other similar numerical codes.

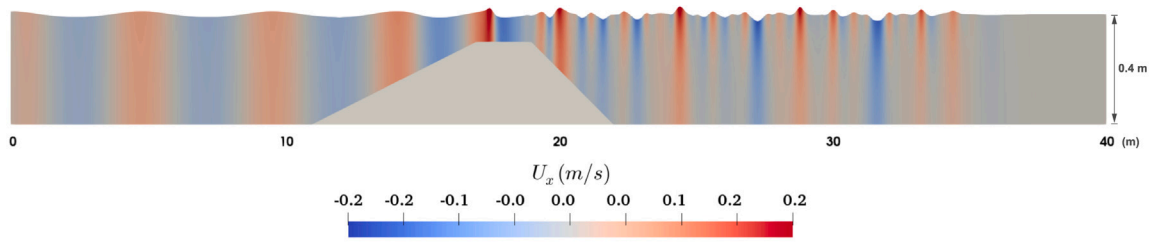


Fig. 9. Horizontal velocity component at $t = 60$ s in the numerical wave tank of wave propagation over a submerged bar (The vertical direction is scaled by a factor of 10 for visualisation purpose).

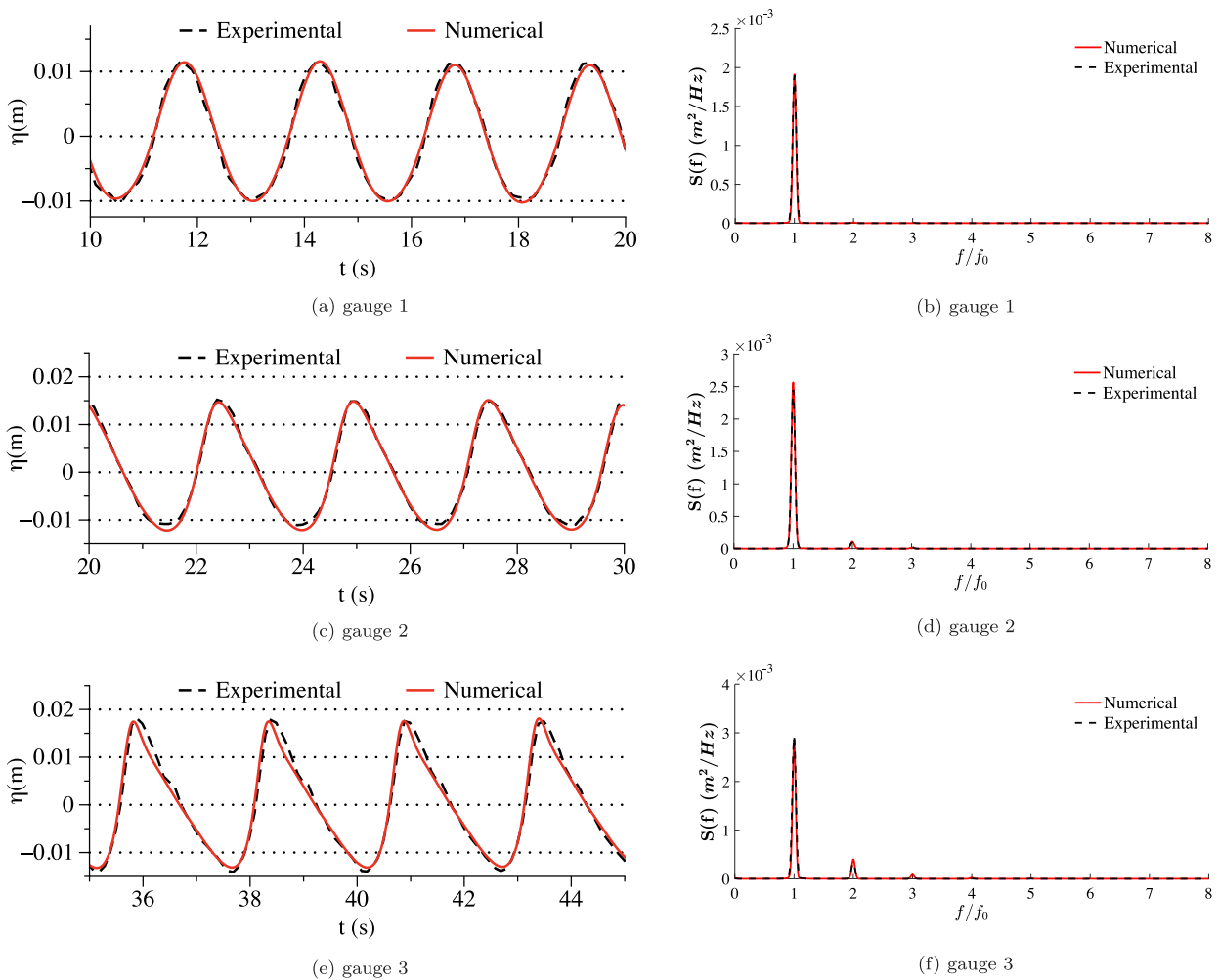


Fig. 10a. Comparison between the numerical results and experimental measurements for the wave transformation over a submerged bar (Part 1).

4. Engineering applications

In this section, two engineering applications are described. The focus is on the effectiveness of the coastline algorithm for complicated shorelines. Norway has a long coastline with complicated coastline geometry due to the fjords and archipelagos. Fig. 25 shows the locations and the surrounding areas of the two sites for simulations along the Norwegian coast. With these different and challenging coastal topographies, the coastline algorithm is evaluated.

4.1. Harbour design at mehamn

The first application is the investigation of the wave conditions inside the Norwegian harbour Mehamn. Mehamn is the north-most

harbour that the passenger ferry service Hurtigruten travels to. The harbour is surrounded by two peninsulas to the east and west but open to ocean swell at the north side. Intermediate to shallow water conditions are found around and inside the harbour. The satellite image from 2019 and water depth contour map of the harbour and its surrounding area are shown in Fig. 26. The two breakwaters are marked as BW1 and BW2 and the two peninsulas surrounding the harbour are marked as peninsula A and peninsula B.

A model scale experiment with a scale factor of 1:80 was performed for the purpose of breakwater design at the SINTEF Coast and Harbour Laboratory in Trondheim (Vold and Lothe, 2009). In the experiment, the water depth was truncated at 40 m in full scale and 0.5 m on the experiment scale. Only part of the inlet boundary from $x = 0$ to $x = 9.5$ m (760 m in full-scale) is covered by the wave generator, while the rest is blocked by a solid object, as seen in Fig. 27. Nine wave gauges

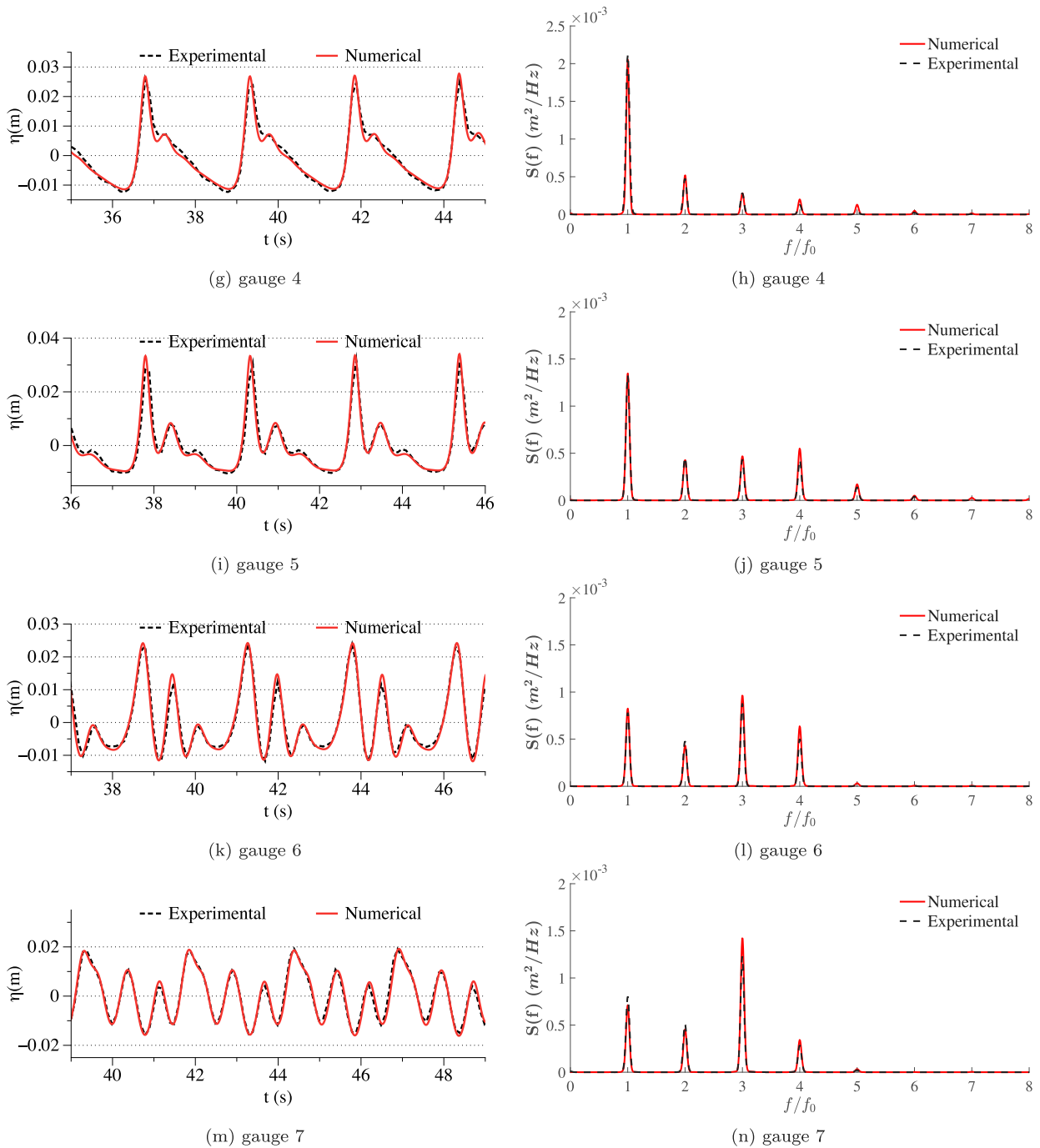


Fig. 10b. Comparison between the numerical results and experimental measurements for the wave transformation over a submerged bar (Part 2).

are arranged in the basin: one wave gauge outside the entrance of the harbour in order to calibrate the incoming waves and eight inside the harbour. The physical experiment configuration is shown in Fig. 27

The proposed numerical model is used to reproduce the results in the experiment that are converted to full-scale. The full-scale topography in Fig. 26a is included in the numerical wave tank as shown in Fig. 28a. The topography is oriented so that the principal wave direction is 14° north-northeast, the same as in the experiment (Vold and Lothe, 2009). The numerical domain is 1760 m long in the north–south direction, and 1440 m in the west–east direction. The maximum water depth is 40 m, corresponding to the experiment. In the simulation, unidirectional irregular waves are generated with a relaxation method at the north boundary (orange box in Fig. 28b) to represent ocean swell propagation into the harbour. Following the experiment (Vold and

Lothe, 2009), the wave gauges in the numerical wave tank are shown in Fig. 28b. The theoretical input significant wave height is 3.5 m and the peak period is 12 s. Wave gauge 1 is used for the calibration of the input wave in the experiment as well as in the numerical wave tank. After iterative trials, the input wave height is modified in order to obtain a 3.5 m significant wave height at wave gauge 1. The slight increase of wave height at a gauge 1 in comparison to the wave generation boundary is largely due to the local shoaling effect. The JONSWAP spectrum (DNV-GL, 2011) with a peak enhance parameter 3.0 is used as the input power spectrum. A narrow band frequency range between $0.75\omega_p$ and $2\omega_p$ is used in the simulation, where ω_p represents the peak angular frequency.

A 2D simulation is performed first in a numerical wave flume to determine the grid arrangement for a correct representation of the input

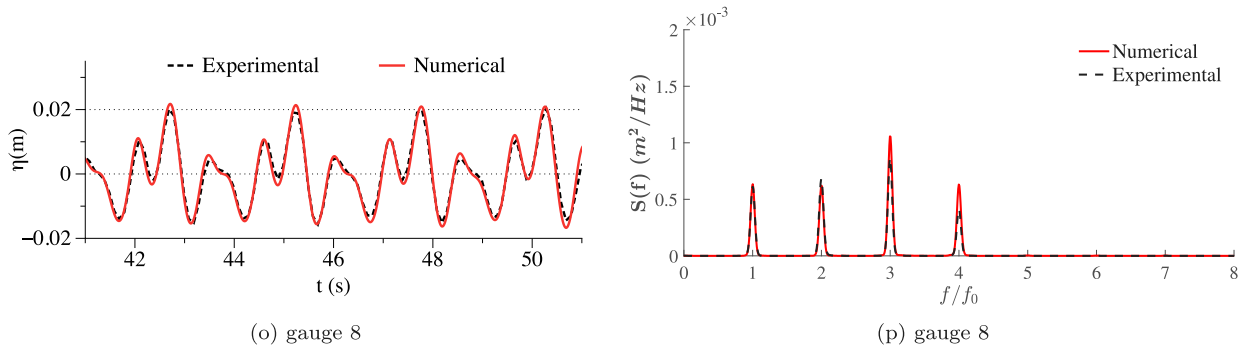


Fig. 10c. Comparison between the numerical results and experimental measurements for the wave transformation over a submerged bar (Part 3). (a)(c)(e)(g)(i)(k)(m)(o) surface elevations at 8 wave gauges at $t = 60$ s, (b)(d)(f)(h)(j)(l)(n)(p) frequency spectra at 8 wave gauges. Black lines are from experiments, red lines are results of REEF3D::FNPF. f/f_0 is the normalised frequency and f_0 is the frequency of the input wave, $f_0 = 1/2.525$ Hz. The grid size $dx = 0.02$ m and $CFL = 1.0$.

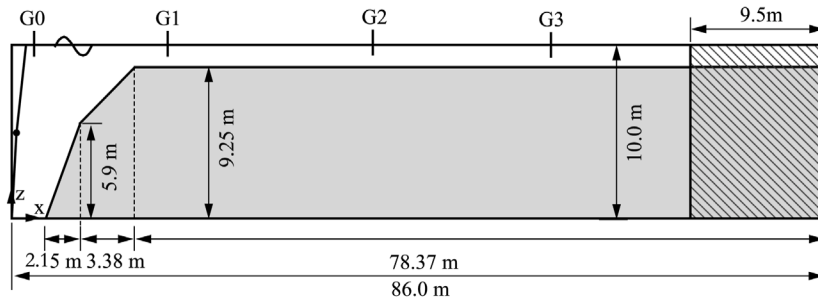


Fig. 11. Numerical wave tank setup for wave propagation over a steep ramp.

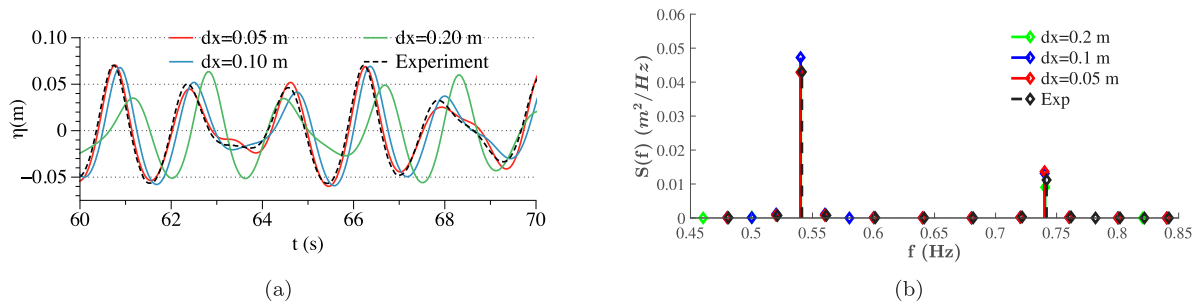


Fig. 12. Grid convergence for the simulation of bi-chromatic wave propagation over a steep ramp. (a) time series of free surface elevation at wave gauge G2, (b) frequency spectra at wave gauge G2.

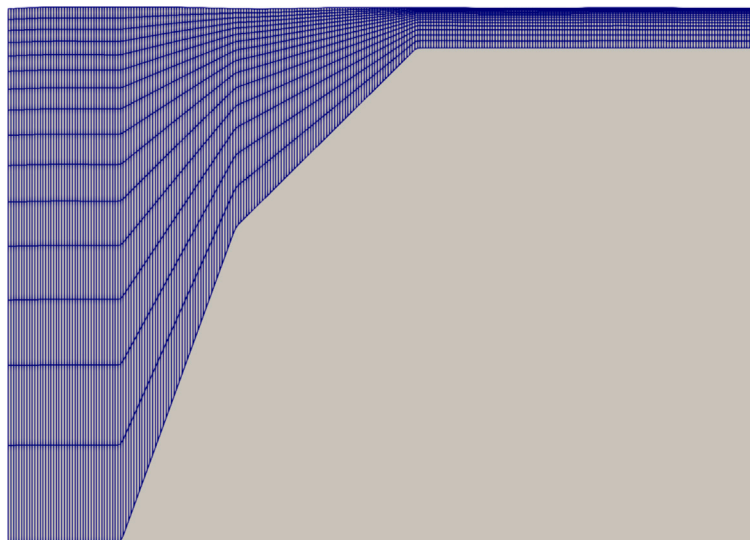


Fig. 13. σ -coordinate at the steep slope in the simulation of wave propagation over a steep ramp with the horizontal cell size 0.05 m and 15 cells and a stretching factor of 3.0.

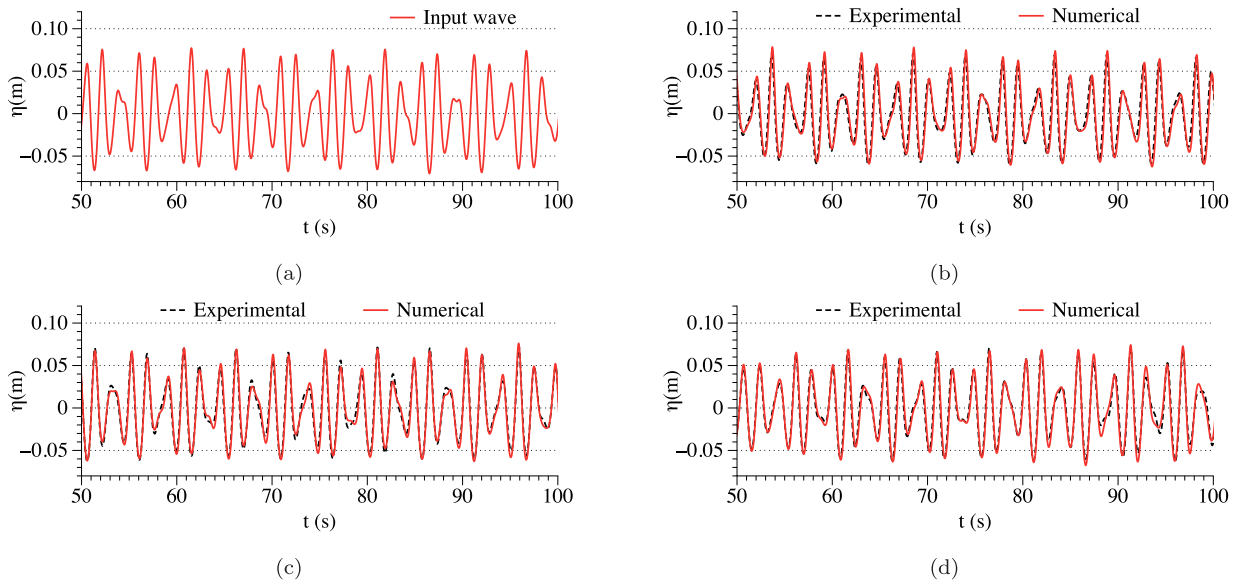


Fig. 14. Comparison of free surface time series between the simulated waves and experimental measurements. (a) the input wave signal in the numerical simulation at G0. (b)–(d) surface elevation time series at G1, G2 and G3.

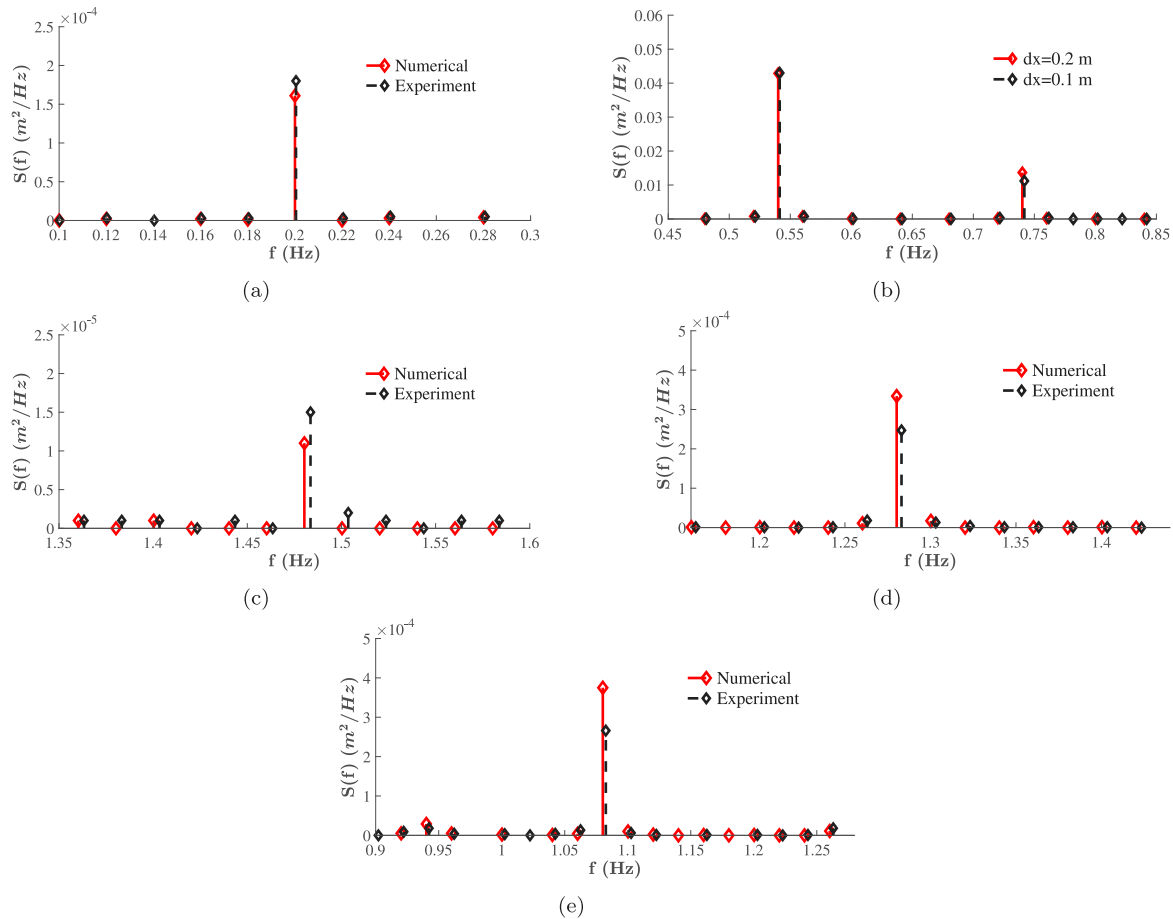


Fig. 15. Frequency spectra at wave gauge G2 in the simulation of bi-chromatic wave propagation over a steep ramp, (a) frequency spectrum near ω_3 , (b) frequency spectrum near ω_1 and ω_2 , (c) frequency spectrum near ω_4 , (d) frequency spectrum near ω_5 , (e) frequency spectrum near ω_6 .

wave spectrum. 10 cells in the vertical direction with a stretching factor of 2.0 is used based on the constant-truncation error method for the water depth in the offshore region. 12 800 s simulations are performed and the surface elevation time histories between 2000 s and 12 800

s at $x = 300$ m are used to calculate wave spectra. $x = 300$ m is located right after the wave generation zone to ensure the input wave quality. The simulated spectra are compared with the theoretical one in Fig. 29. The spectrum obtained with $dx = 4$ m agrees with the

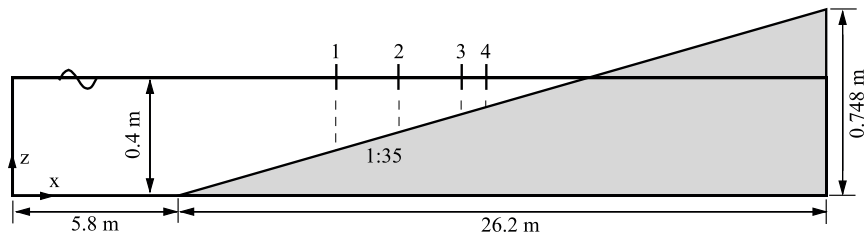


Fig. 16. Numerical wave tank setup for wave breaking over a mild slope.

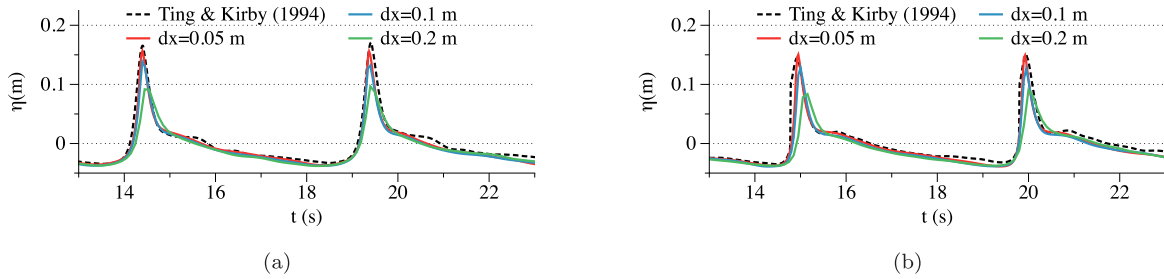


Fig. 17. Grid convergence for the simulation of wave breaking over a mild-slope. (a) time series of surface elevation at wave gauge 2, (b) time series of surface elevation at wave gauge 3. 2-cell size coastal zones are used in all simulations.

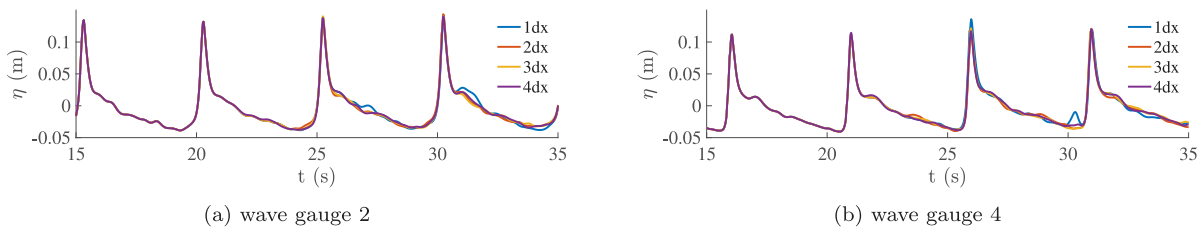


Fig. 18. Coastal zone width convergence study in the simulations of wave breaking over a mild slope.

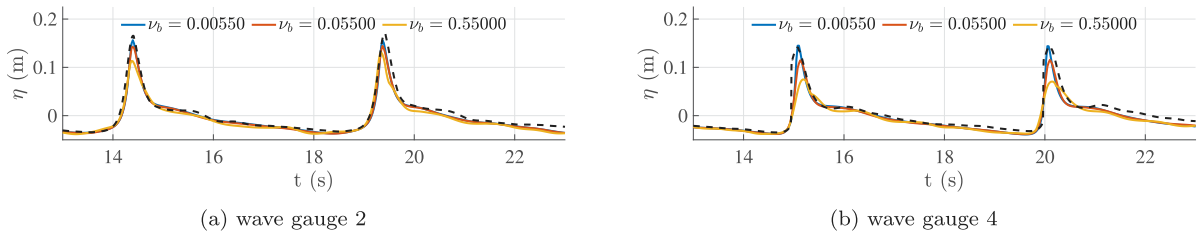


Fig. 19. Sensitivity study on the viscous damping factor ν_b in the breaking algorithm in the simulations of wave breaking over a mild slope. The black dashed lines represent the experimental measurements.

theoretical input wave spectrum at the peak frequency as well as at the low-frequency end and high-frequency end. Further refinement of the grid results in a similar spectrum without obvious further improvement. Therefore, a horizontal cell size of $dx = 4$ m is used in the following simulations. The coastal zone width convergence study is performed to choose the minimum width that does not have a significant influence on the wavefield while eliminating the swash zone instability. The wave spectra at wave gauge 3 near the inlet of the harbour and wave gauge 8 near the marina inside the harbour are compared using different coastal zone widths, as shown in Fig. 30. It is seen that when only one cell is used for the coastline width, the spectra are significantly different from other results at both gauges due to the instability in the swash zone and unphysical run-up and run-down. When a coastal zone size of 2 cells and 3 cells are used, the reproduced spectra are very similar at both locations, especially near the peak frequencies. With the increasing width of the coastal zone, the spectra peaks decrease monotonically at both gauges. Similar to the finding of Section 3.4, a 2-cell coastal zone width is used in the following simulations.

With a cell size of 4 m in the horizontal direction and 10 cells in the vertical direction, the total number of cells is 1.584 million for the full-scale 3D Mehann simulation. The simulation is performed for 12800 s and the time series of surface elevation between 2000 s and 12800 s is used for the calculation of significant wave heights inside the harbour. The 12800 s simulation takes 7.9 h to finish using 128 Intel Sandy Bridge processors (2.6 GHz) on the supercomputer Vilje. With the same numerical configurations, investigations are also made to study the effects of the breakwaters. In total, four scenarios are compared: without breakwaters, with only breakwater BW1, with only breakwater BW2 and with both breakwaters. The surface elevations at $t = 12800$ s in all four simulations are shown in Fig. 31.

Strong wave refraction and diffraction are observed at the tips of the two peninsulas. The water depth variations at the tips of the two peninsulas cause the wave direction to bend towards the coast due to refraction. This process continues along the coastline of the two archipelagos, guiding the waves into the interior of the harbour. Another phenomenon that leads the incoming waves into the harbour

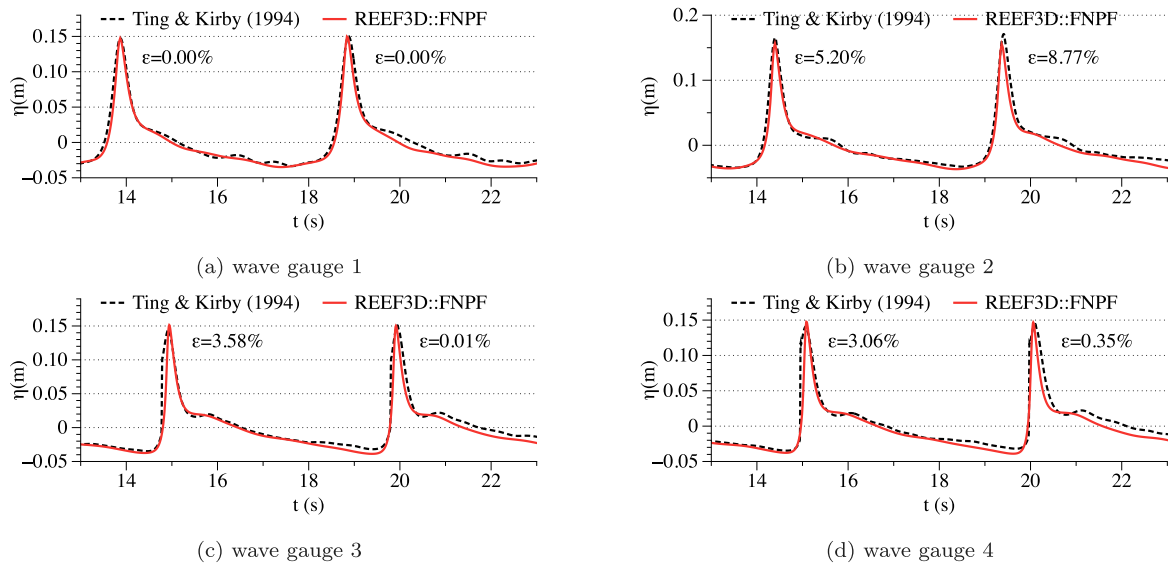


Fig. 20. Time series of surface elevation and relative errors of wave crest height at all four wave gauges in the simulation of wave breaking over a mild-slope.

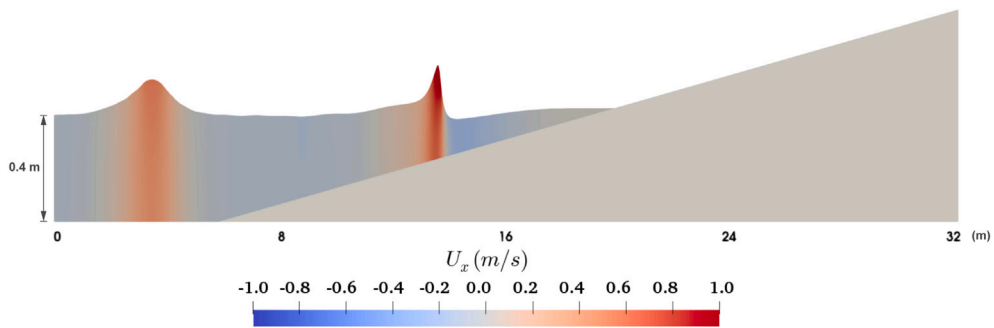


Fig. 21. Breaking wave at $t = 10.75$ s. The wave crest increases to its maximum and the wave front becomes vertical. The horizontal velocity also reach the maximum at the wave crest (The vertical direction is scaled by a factor of 10 for visualisation purpose).

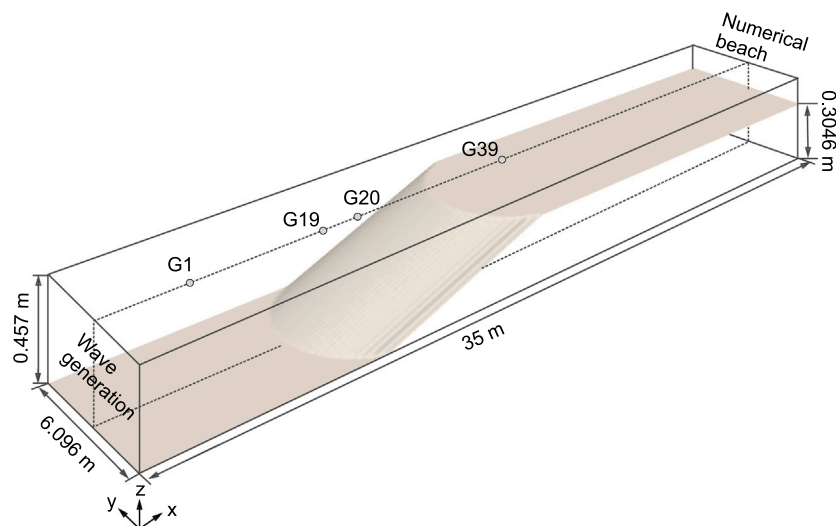


Fig. 22. Numerical wave tank setup for the three dimensional wave shoaling over a semi-circular submerged reef.

is diffraction. Diffraction first takes place at peninsula B and causes the incoming waves to change direction and to propagate towards the inner harbour. Both the input wave and the diffracted wave around peninsula B meet at peninsula A and diffraction takes place in association with a strong shoaling effect at the tip of peninsula A. As a result of the

combination of refraction and diffraction, the swell propagates around the peninsulas and spreads in the entire inner harbour. The breakwaters block the refraction process along the coastlines of peninsulas A and B respectively and prevent the waves from being guided towards the inner harbour. The strong diffraction pattern persists after breakwater

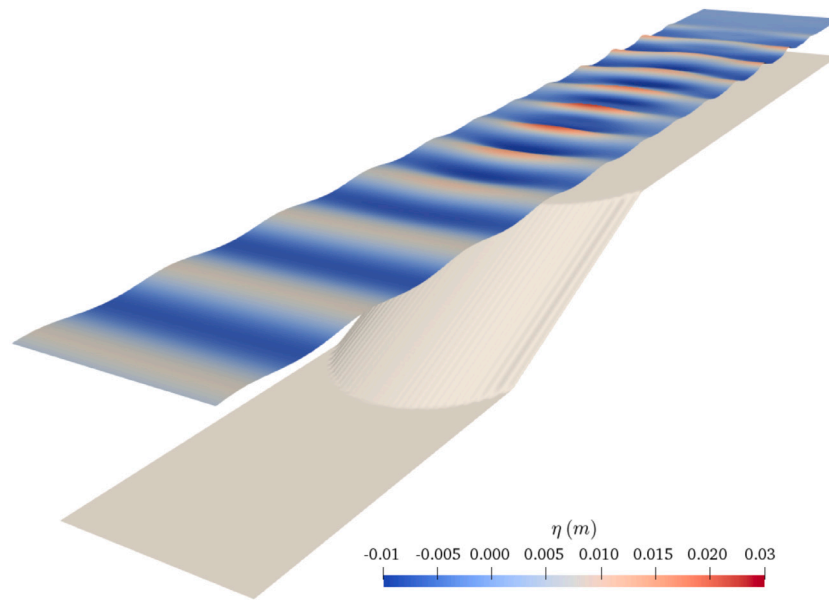


Fig. 23. Surface elevation over the entire numerical wave tank of three dimensional wave shoaling over a semi-circular submerged reef at $t = 100$ s (The numerical domain is amplified 10 times in the vertical direction for the purpose of visualisation).

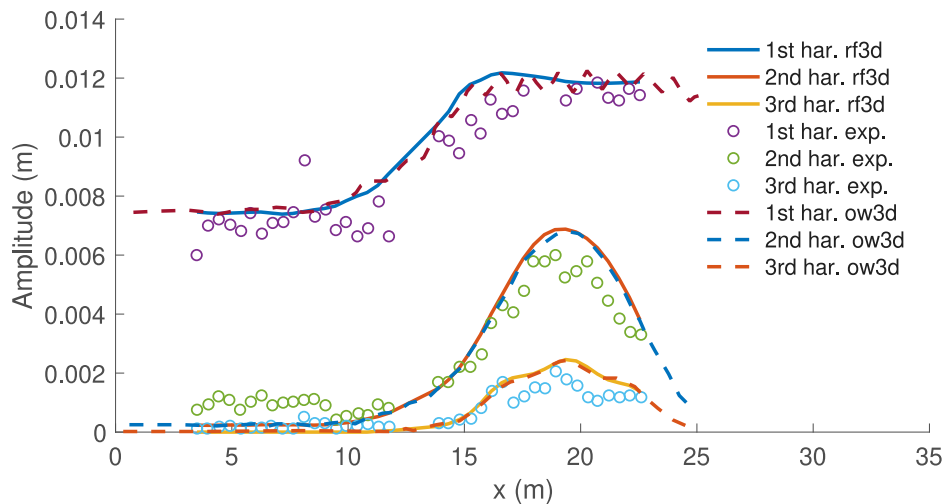


Fig. 24. Comparison of the three wave harmonics in the measurements, REEF3D:FNPF simulation and OceanWave3D simulation along the centreline of the three dimensional wave shoaling experiment by Whalin (1971). 'exp.' represents the experimental measurements (Whalin, 1971), 'ow3d' represents the OceanWave3D simulations (Engsig-Karup et al., 2009) and 'rf3d' represents the REEF3D:FNPF simulation.

BW1 is installed. The diffraction around peninsula A dominates the wave propagation into the harbour. However, waves along the east side of the harbour are reduced. Therefore, the infrastructures along the east coastline are better protected. BW2, on the other hand, decreases the diffraction at peninsula A significantly. Consequently, much smaller waves are observed in the inner harbour. The combined use of the two breakwaters is seen to reduce both the wave height along the east side of the harbour as well as in the inner harbour.

In the physical experiment, the scenario with no breakwater and the scenario with both breakwaters were tested. The significant wave heights at all nine wave gauges obtained in the numerical wave tank are then compared to the experiment for both scenarios in Figs. 32a and 32b:

It is seen that H_s at all wave gauges as well as the general trend of wave height variation in the inner harbour agree well between the numerical simulations and the experiments for both scenarios. This proves that the coastline algorithm captures the complex wave transformation near and inside the harbour. A correct representation of

the wave diffraction ensures an accurate calculation of the wave height at the gauges 5 to 9. A quantitative comparison of the simulated effects of the breakwaters is seen in Fig. 33.

The visual observation in Fig. 31 is confirmed in Fig. 33. It is seen that the significant wave heights at all wave gauges inside the harbour are significantly reduced after waves pass the two breakwaters BW1 and BW2 in Fig. 26a. Breakwater 2 has a much stronger effect than breakwater 1 on reducing wave height at nearly all wave gauges. However, the combined usage of the two breakwaters further reduces the wave height at wave gauges 6,7 and 9. In fact, most small leisure boats and fishing boats are docked in the marina near wave gauge 9. The combined usage of the breakwaters proves to be necessary in order to protect the small boats from large motions.

The study of Mehamn harbour shows the model's capability to represent complicated wave transformation over natural bathymetry. Strong diffraction near complex coastlines and breakwaters are well represented. The computational time is only twice that of real-time with affordable computational resources. The computational efficiency

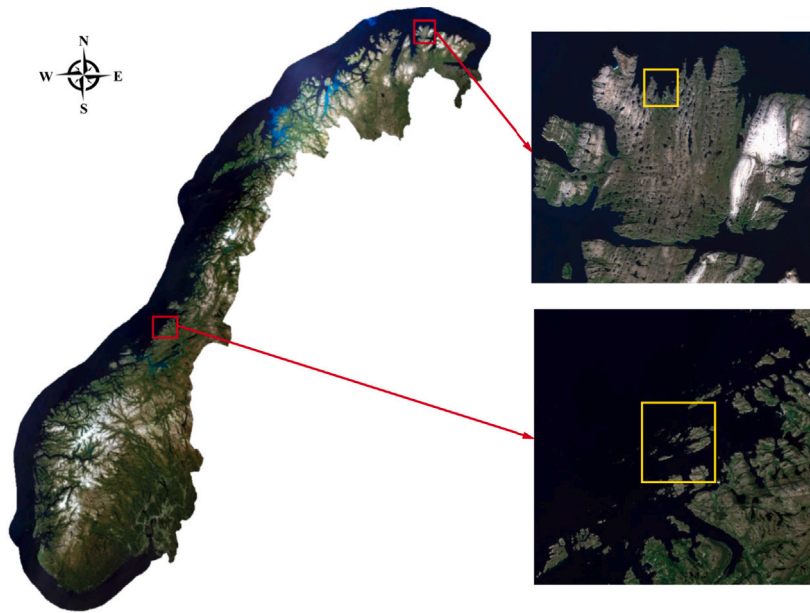


Fig. 25. Locations and surrounding areas of the two engineering application sites in the Norwegian coast (Statens kartverk, 2020). The red and yellow boxes in the north of the map show the Mehamn harbour location and its adjacent area. The red and yellow boxes in the north of the map show the planned Flatøya fish farm location and its adjacent area.



Fig. 26. Mehamn harbour: (a) satellite image; (b) water depth contour. The two breakwaters are marked as BW1 and BW2 and the two peninsulas are marked as A and B.

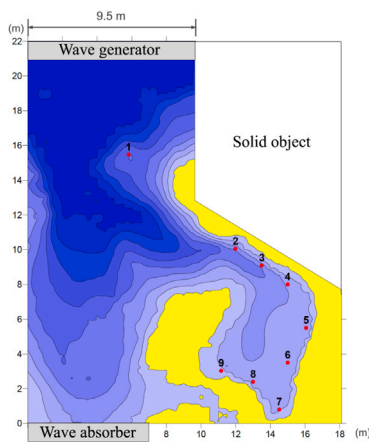


Fig. 27. Configuration of the physical experiment for Mehamn harbour (Vold and Lothe, 2009). The grey shaded area at the upper boundary is the wavemaker, the white-grey shaded area at the lower boundary is the wave absorber.

enables the model for large-scale engineering applications. The model is seen to be a suitable tool for harbour planning and analysis of coastal infrastructures and coastal protection. The coastline algorithm has shown to be a pragmatic methodology that helps to capture the correct large-scale statistical characteristics of the flow field with the presence of complex coastline geometries.

4.2. Aquaculture site analysis at Flatøya

As mentioned in Section 3.2, it is challenging to represent de-shoaling processes in shallow water models, but REEF3D::NPPF was able to represent accurately the wave shoaling and de-shoaling in a 2D simulation of wave propagation over a submerged bar. In this section, the wave conditions at a planned fish farm site and its surrounding area are simulated. The fish farm site is located near the Flatøya island in Norway. In this scenario, waves from the offshore area propagate over a very shallow region filled with an archipelago before reaching the fish farm site, where the water depth suddenly increases significantly. The presence of the archipelago creates complicated wave diffraction and reflection in addition to the strong shoaling and de-shoaling phenomena. The terrain map of the area near the fish farm is shown in Fig. 34a where the fish farm site is shown as a red box. The offshore area has

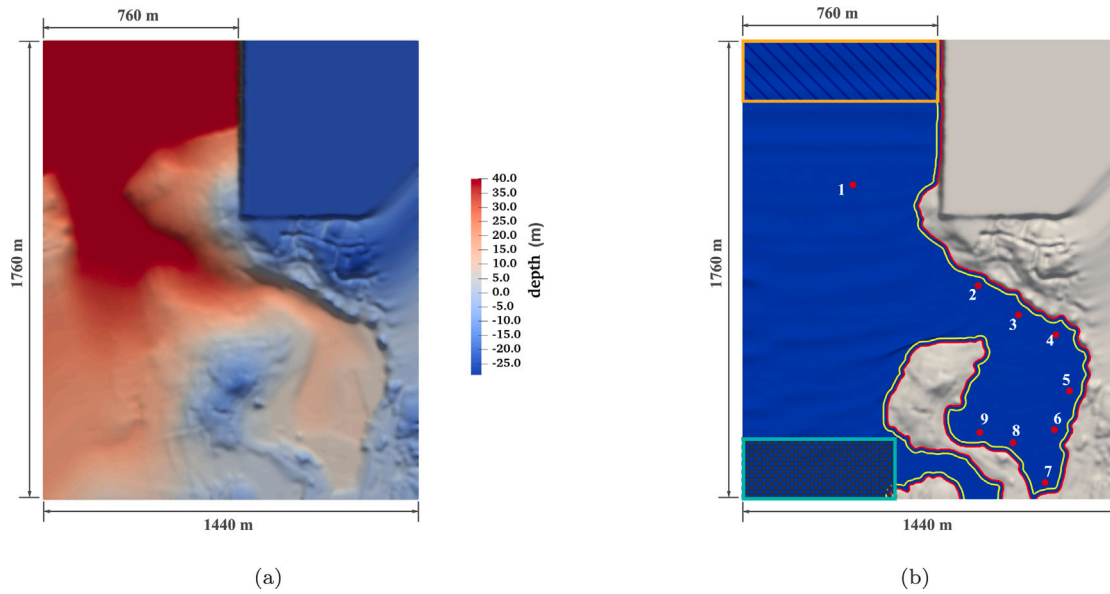


Fig. 28. Configuration of the simulation of wave propagation in Mehamn harbour. (a) the bathymetry of Mehamn harbour, negative values indicate areas above water level. The bathymetry is truncated at 40 m water depth, as seen in the solid red area; (b) the orange box is the wave generation zone, the cyan box is a numerical beach, the red lines show the coastlines detected in the model and the yellow lines show the outer boundaries of the coastal relaxation zones. All the topography are vertically scaled with a factor of 3 for visualisation purposes.

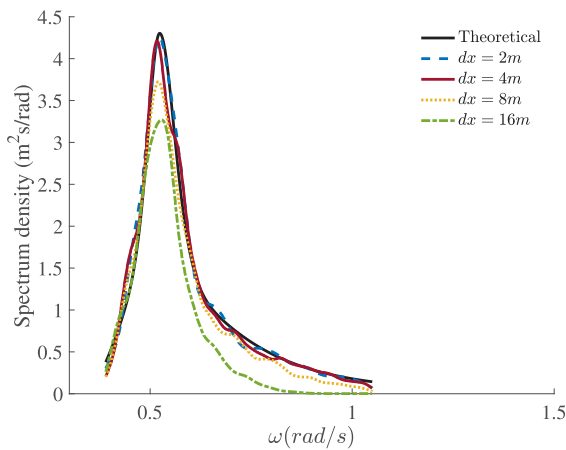


Fig. 29. Comparison of spectrum density at the wave gauge $x = 300$ m in the 2D simulation with the input wave for Mehamn harbour.

a characteristic water depth of 300 m, and a shallow water region of an average 20 m water depth lies in between the offshore region and the fish farm. The water depth around the fish farm is about 200 m. A close-up view of the fish farm is shown in Fig. 34b. The fish farm is located right behind the Flatøya island. Here, each cell represents a fish cage and each grid point represents a floating buoy, which is moored to the seabed. In the following simulation, the wave gauges are arranged at the locations of the 50 floating buoys in the fish farm.

The black box in Fig. 34a shows the chosen simulation domain. The longitudinal dimension is 14 km (north-west to south-east direction) and the transverse dimension is 7 km (south-west to north-east direction). Uni-directional irregular waves are generated from the offshore boundary with 300 m water depth from the north-west 45 degree direction. The input wave has a significant wave height of $H_s=2.5$ m and a peak period of $T_p = 15$ s. A JONSWAP spectrum (DNV-GL, 2011) with a peak enhance factor 3.0 is used as the input power spectrum. The frequency range from half of the peak frequency to double that of the peak frequency $[0.5\omega_p, 2\omega_p]$ is used in all following simulations.

The numerical domain is arranged so that the wave direction is perpendicular to the wave generation boundary. The configuration of the numerical wave tank is shown in Fig. 35, the domain length is 14 000 m in the x -direction and 7000 m. The red box is the wave generation zone. Numerical damping zones are arranged along the other three boundaries to eliminate the interference of wave reflections from the boundaries. The red and yellow circles show the locations of the wave gauges, which correspond to the grid points in Fig. 34b.

First, a 2D numerical wave flume which is 14 000 m long is used for the grid convergence study. 10 cells in the vertical direction with a stretching factor of 2.0 is used following the method described in Section 2.2 based on the water depth in the offshore region. 12 800 s simulation time is used and the surface elevation time histories between 2000 s and 12 800 s at $x = 7000$ m are used to calculate the wave spectra. $x = 7000$ m is at the centre of the tank and before the waves reach the archipelago, where the wave quality must be ensured. The simulated spectra are compared with the theoretical one in Fig. 36. The spectrum obtained with both $dx = 10$ m and $dx = 5$ m agrees with the theoretical input wave spectrum at both the peak frequency and the low-frequency and high-frequency ends. The result from $dx = 5$ m does not further improve the representation of the spectrum so that $dx = 10$ m is chosen for all the following stimulations. With the chosen grid arrangement, the resulting number of cells in the simulations is 9.8 million. Following the finding from Section 4.1, a 2-cell coast zone width is used in the simulations.

As mentioned previously, phase-resolved models have the advantage in representing some of the strongly nonlinear wave transformation processes such as strong diffraction in comparison to spectral wave models. In this scenario, the archipelago creates a strong diffraction pattern, especially around Flaøya. In order to verify and demonstrate this advantage of the proposed phase-resolved wave model, the widely used third-generation spectral wave model SWAN (Booij et al., 1999) is used to simulate the same fish farm site.

A grid convergence study of SWAN (Booij et al., 1999) is also performed. For a spectral wave model, the grid resolution requirement for the offshore area is not as strict as a phase-resolved model. However, sufficient resolution at the wave diffraction area is required. The H_s at the 10 yellow wave gauges in Fig. 35 are used for the grid convergence study. The H_s obtained when using different cell sizes are compared in

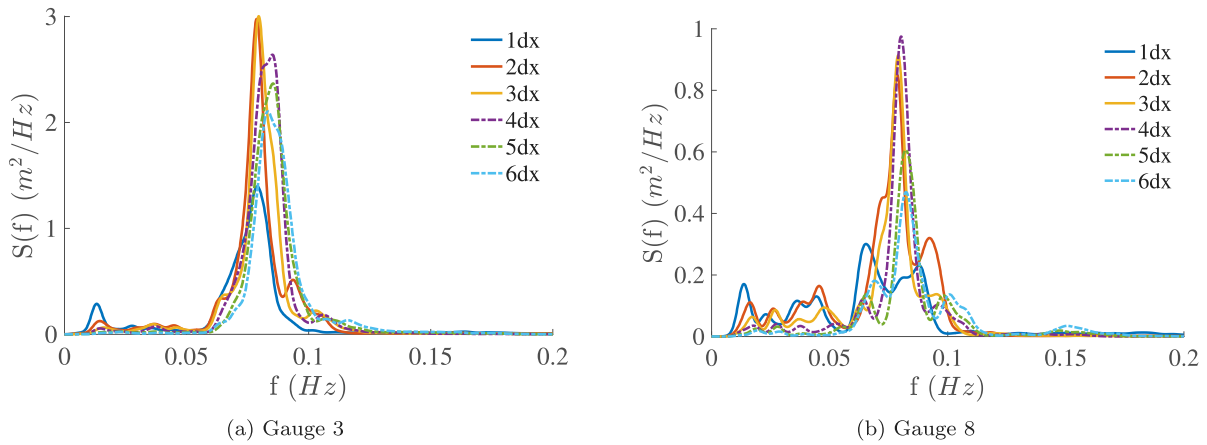


Fig. 30. Frequency spectra at wave gauge 3 and 8 using different coastal zone width in the simulations of Mehman harbour.

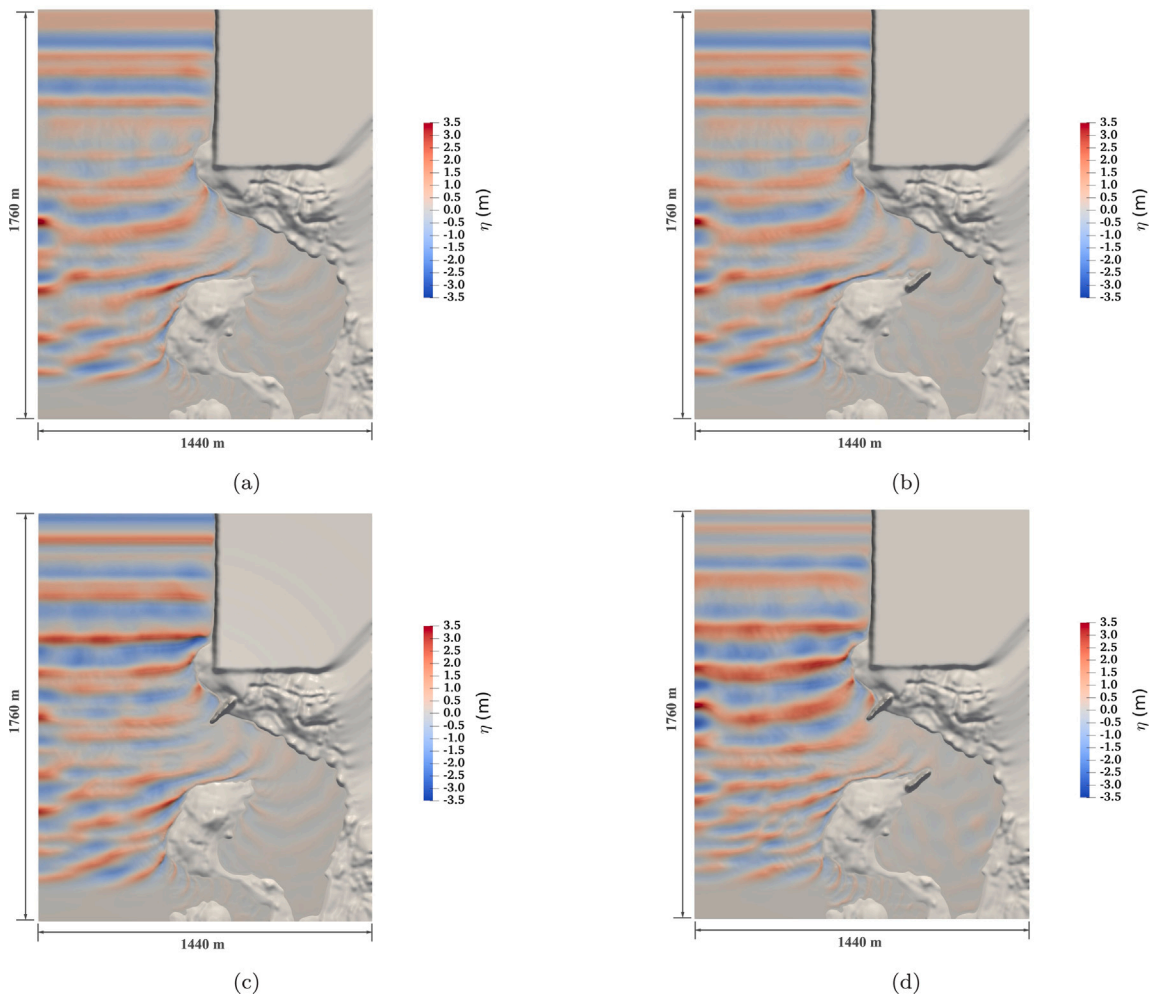


Fig. 31. Free surface elevation in the simulations of wave propagation into Mehman harbour at $t = 12800$ s; (a) without any breakwater, (b) with breakwater BW2, (c) with breakwater BW1, (d) with both breakwaters BW1 and BW2.

Fig. 37. As can be seen, the H_s varies significantly with the refinement of the cell size until a further refinement is made from $dx = 20$ m to $dx = 10$ m, where near-identical results are obtained from both simulations at all ten wave gauges. Therefore, 20 m cell size is used for the comparison with the proposed phase-resolved model.

With the chosen grid resolutions, the surface elevation in the entire numerical wave tank at $t = 12800$ s in the REEF3D::FNP simulation

alongside with the H_s distribution from the SWAN simulation are shown in Fig. 38.

Both simulations show the wave shoaling process when the deep-water waves propagate to the shallow water region between $x = 2000$ m and $x = 6000$ m. After the shoaling and possible wave breaking, the waves start to diffract around the archipelago before reaching the fish

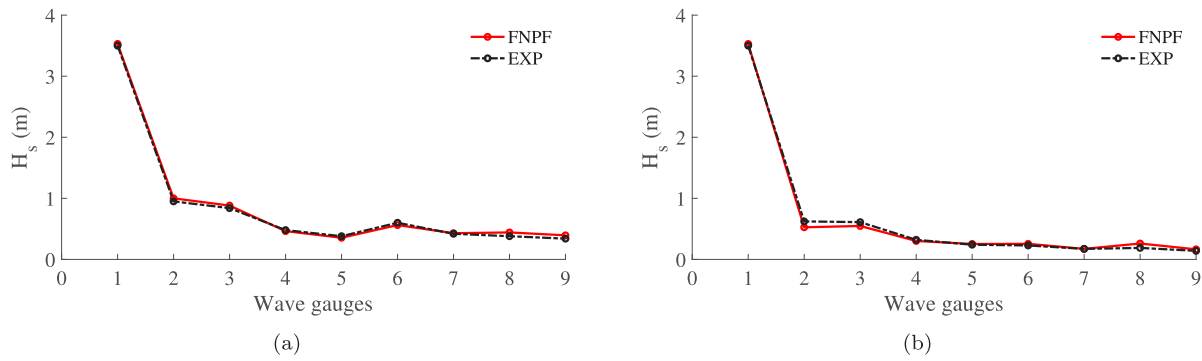


Fig. 32. Comparison of H_s at the wave gauges between the experimental measurements and numerical simulations for (a) wave propagation in Mehamn harbour without breakwaters, (b) with both breakwaters BW1 and BW2.

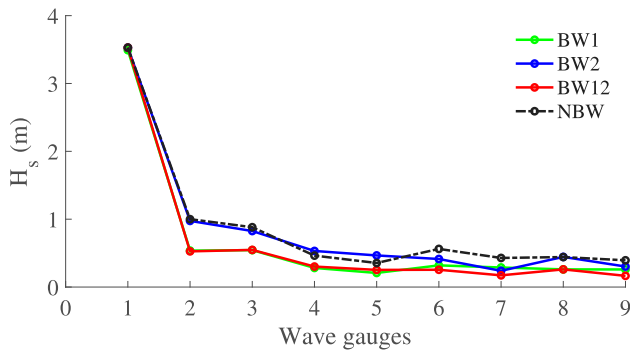


Fig. 33. Significant wave heights at all wave gauges inside the Mehamn harbour in simulations with different breakwater configurations.

farm site, where much smaller waves are seen in comparison to the input waves.

Close-up views near the fish farm show a more clear pattern of strong wave diffraction around Flatøya, as seen in Fig. 39. Waves diffract at both ends of the island and most regions behind the island are not sheltered from incoming waves but filled with the diffracted waves. The two diffracted waves from both ends of the island meet near the fish farm location. Both models show a qualitative confirmation of this wave diffraction pattern.

The spatial distribution of the H_s are compared at the fish farm site as seen in Fig. 40.

The spatial variation of the two models shows a similar pattern and confirms that the strongest wave diffraction comes from the lower end of the island. However, the comparison also show that significantly larger waves are calculated in REEF3D::FNPF in comparison to SWAN. Therefore, a quantitative comparison of the significant wave heights at all 50 wave gauges between the two models is shown in Fig. 41.

It is seen that larger waves are calculated at all wave gauges from the phase-resolved model in comparison to the spectrum wave model. The differences of the simulated wave heights are summarised in Table 1 for the 10 yellow wave gauges. The differences of H_s in percentage at all wave gauges are plotted in Fig. 42. The relative differences are calculated as the absolute differences divided by the corresponding values from REEF3D::FNPF. The wave heights from SWAN are underestimated by 20% to 50%.

As a spectral wave model that solves energy action balance equations, SWAN does not give details on wave kinematics and dynamics and cannot resolve wave diffraction (Booij et al., 1999; Ris et al., 1999). Instead, the phase-decoupled approach by Holthuijsen et al. (2003) is used to show the wave energy spatial distribution and changes in wave direction qualitatively. However, this approach does not properly handle diffraction in front of reflective obstacles such as in harbours (Thomas and Dwarakish, 2015; SWAN, 2016).

Table 1

Differences in calculated H_s in the SWAN and REEF3D::FNPF simulation at the last 10 wave gauges shown as yellow circles in Fig. 35.

Wave gauges	H_s in SWAN (m)	H_s in REEF3D::FNPF (m)	Difference
Gauge 41	0.1810	0.2472	26.8%
Gauge 42	0.2002	0.2902	31.0%
Gauge 43	0.2315	0.3061	24.4%
Gauge 44	0.2210	0.3561	38.0%
Gauge 45	0.2163	0.3924	44.9%
Gauge 46	0.2112	0.2820	25.1%
Gauge 47	0.1912	0.2933	34.8%
Gauge 48	0.2574	0.3370	23.6%
Gauge 49	0.2413	0.3682	34.5%
Gauge 50	0.1867	0.3697	49.5%

There exists unfortunately no in-situ measurement at Flatøya for comparison. The challenge in representing strong diffraction when using a phase-averaged model (Thomas and Dwarakish, 2015) is possibly the main reason behind the differences in the results. Though it is difficult to confirm the reasoning due to the lack of measurements, a cross-check of numerical models is recommended for coastal wave simulations with strong diffractions.

5. Conclusions

In the presented manuscript, the fully non-linear potential flow model REEF3D::FNPF is introduced as a model dedicated to coastal wave modelling in challenging hydrographic environments. The model applies high-order discretisation schemes for the free-surface boundary condition, a second-order scheme for the Laplace solver and uses MPI for multi-core parallel computation. These implementations ensure highly accurate and computationally efficient numerical modelling of wave propagation. Flexible wave generation methods are implemented for versatile applications from experimental scale to full-scale simulations. A relaxation wave generation method is used for general wave generations, a double-hinge flap wavemaker is used to reproduce experimental-scale time series in Section 3.3 and a Neumann boundary is used to reproduce the experimental configurations in the NWT in Section 3.4. The σ -coordinate arrangement allows the vertical grid to follow the topographic variations and steep slopes at the seabed, enhancing the flexibility of wave modelling over varying bathymetry from deep water to shallow water. The breaking wave algorithm detects breaking waves and dissipates wave energy at various water depths using the chosen parameters according to best practices as documented in the literature. The coastline algorithms eliminate the swash zone instability due to infinitesimal water depth while minimising the influence of the flow field. The numerical model reproduces the wave propagation well in all tested validation cases. In Section 3.1, the model shows an accurate representation of the steep 5th-order Stokes wave surface elevation and flow information. The simulations of wave

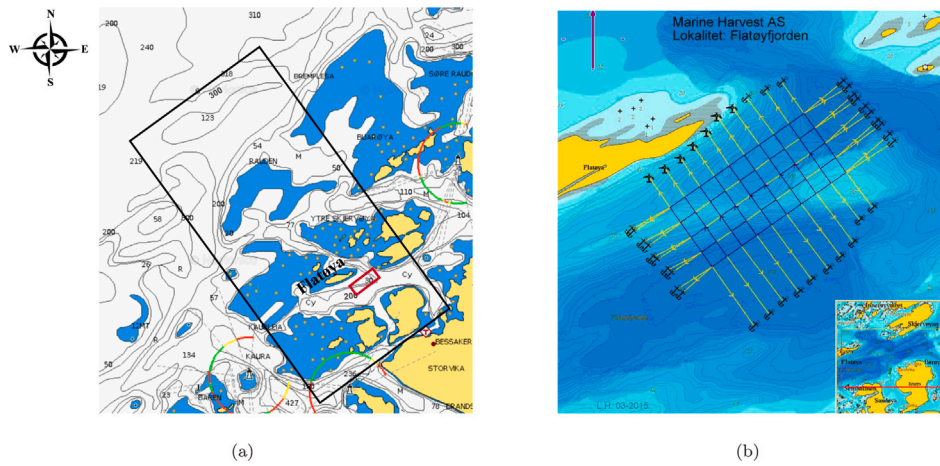


Fig. 34. Flatøya and the fish farm. (a) Topography around the fish farm (red box). The simulation area is shown as the black box. The input wave comes from the north-west boundary corresponding to 300 m water depth. (b) The fish farm arrangement (Hagen, 2015). Every grid point is a floating buoy as well as a wave gauge in the numerical wave simulation.

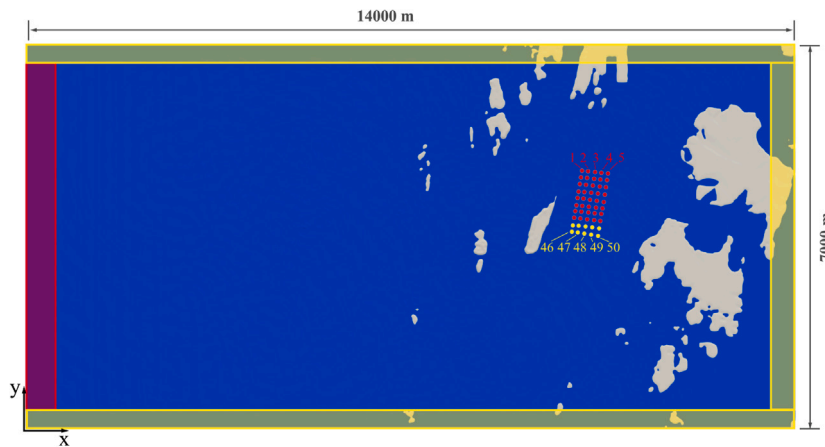


Fig. 35. Numerical wave tank in the simulations of REEF3D::FNPF and SWAN for wave propagation near Flatøya. The red boxes show the wave generation zone, while the yellow boxes are the numerical damping zones. The red and yellow circles are the locations of the wave gauges. The wave gauge numbers start from the north-most row from west to east. All wave gauges are used to compare significant wave height distribution at the fish farm area. The yellow circles are also used for the grid convergence of SWAN simulations and the analysis of the differences between SWAN and REEF3D::FNPF.

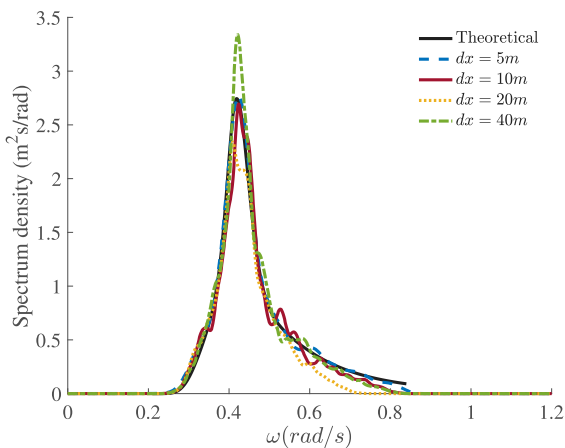


Fig. 36. Grid convergence study for the input wave into Flatøya in 2D.

propagation over a submerged bar and the bi-chromatic wave propagation over a steep ramp (slope larger than 45°) show good agreement between the numerical results and the experimental measurements, including the de-shoaling process and the amplitudes of the emerging bounded wave components. The wave breaking algorithm represents correct wave energy dissipation for a plunging wave breaker as shown in Section 3.4. The simulation of wave shoaling over a semi-circular reef shows an accurate representation of different wave harmonics in a nonlinear 3D scenario.

The novel coastline algorithm introduces a combination of three steps to ensure that the complicated coastlines and the associated wave transformation phenomena are well represented while maintaining a simple and straightforward structured grid in the horizontal plane. The relaxation zones along the coastlines make the coastal reflection property customisable. In addition, the possible numerical instability in the free surface boundary condition at the very shallow water region is avoided. As a result, the model is able to include complicated topography with high flexibility without compromises on numerical stability and computational efficiency. The sensitivity of the coastal zone size is demonstrated and it is found that two cells are sufficient to eliminate numerical instability in the swash zone while maintaining the characteristics of the coastline geometry and thus minimising the influence

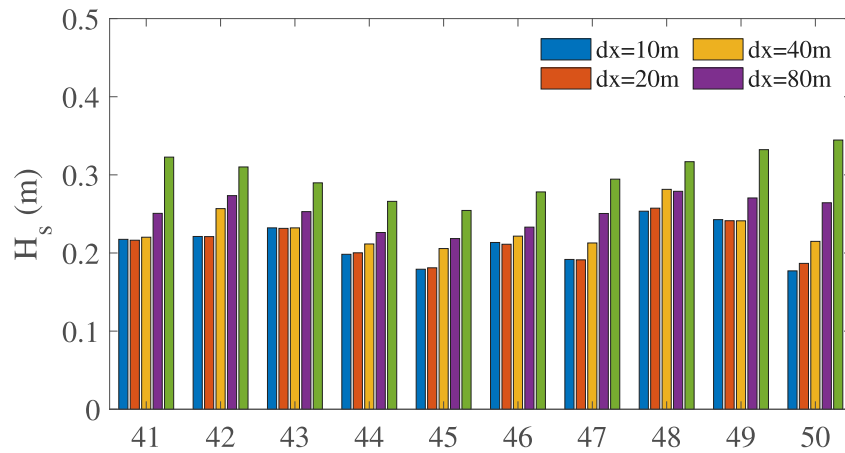
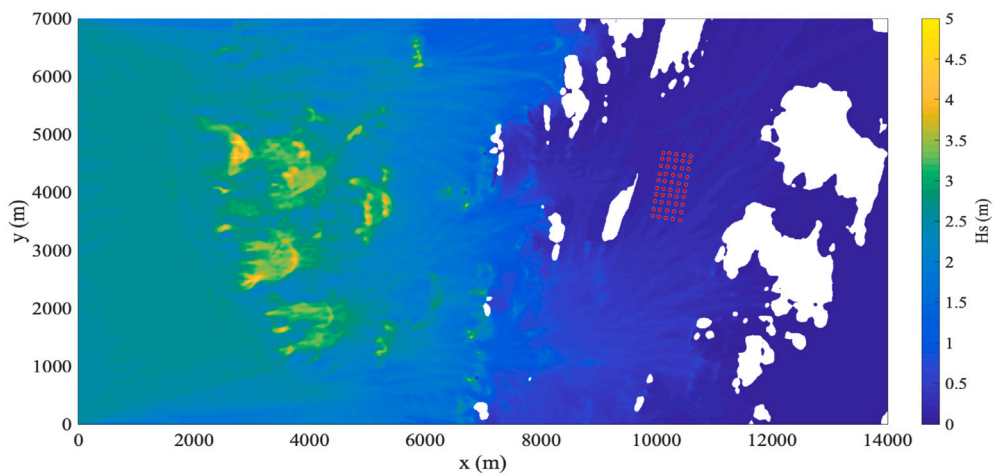
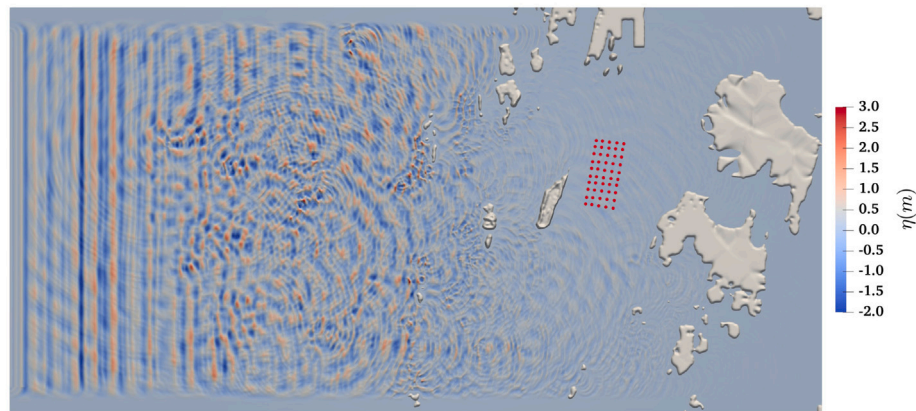


Fig. 37. Grid convergence study for the input wave into Flatøya with SWAN at the south most 10 wave gauges. N_p is the wave gauge number.



(a)



(b)

Fig. 38. Wave field from the simulations of wave propagation from offshore to the fish farm site near Flatøya. (a) distribution of H_s in the SWAN simulation, (b) surface elevation at $t = 12800$ s in the REEF3D::FNPF simulation. The simulation results are magnified by a factor of 10 in the vertical direction for visualisation purpose. The red dots are the locations of the wave gauges in both figures.

on the flow field. The simulations of the wave propagation at Mehamn harbour are compared with experiments and confirm the large-scale performance of the model and its multi-core computational efficiency.

The simulation of the wave propagation near Flatøya shows the model's capability to handle both complex coastline and bathymetry at the same time. The phase-resolved nature of the model contributes to a possibly

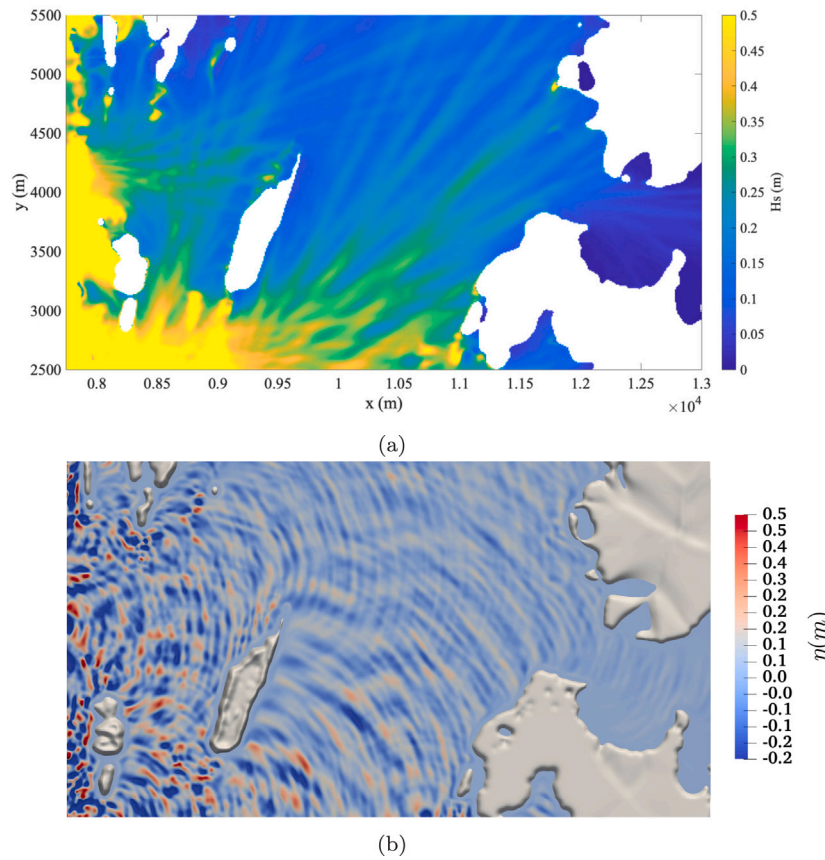


Fig. 39. Wave field in the vicinity of the fish farm near Flatøya. (a) distribution of H_s in the SWAN simulation, (b) surface elevation at $t = 12800$ s in the REEF3D::FNPF simulation. The simulation results are magnified by a factor of 10 in the vertical direction for visualisation purpose.

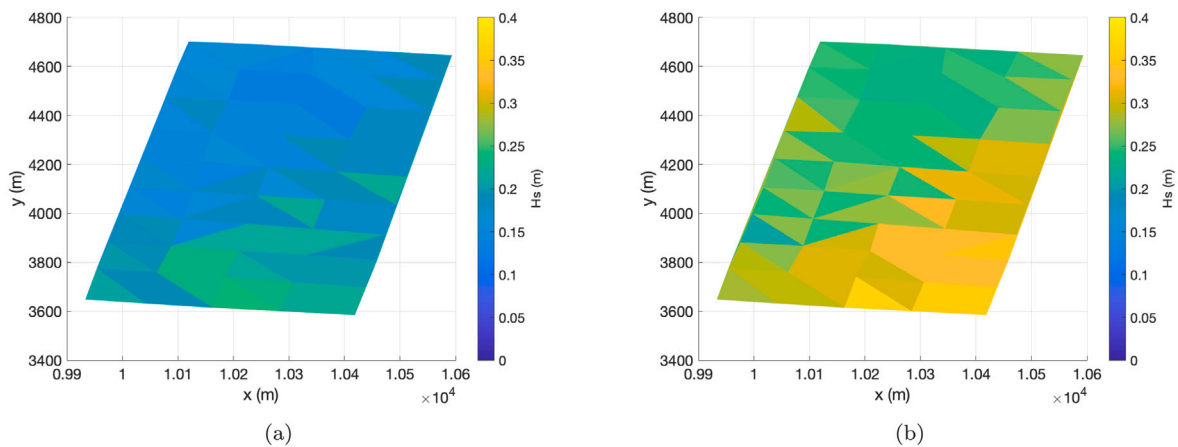


Fig. 40. H_s distribution at all 50 wave gauges covering the fish farm site. (a) SWAN, (b) REEF3D::FNPF.

more accurate representation of the wave condition in comparison to a spectral wave model when strong diffraction is present. Though the details within the swash zone are not resolved, the wave energy is dissipated near the coastlines. This approach shows satisfactory results in representing wave propagation and transformations in the presented coastal scenarios. Though the algorithm does not resolve the physics of the dynamics near the coastlines, it is a useful technique to ensure the correct representation of the complex coastline geometries and to ensure stable simulations over large spatial and temporal scales in a potential flow theory-based NWT. The energy-based coastline algorithm might not be sufficient for specific studies on coastal dynamics, continuous future development of the coastline algorithm is suggested for

improved and more detailed representation of the near-shore processes with further validations.

In conclusion, the proposed fully nonlinear potential flow model and the coastline algorithm provide a working framework for coastal wave modelling in complex coastal environments, considering accuracy, flexibility and efficiency. The numerical model demonstrates its readiness for both experimental validation and large-scale engineering scenarios. In the future, the authors intend to keep updating this working framework with the newest developments regarding breaking algorithms, shoreline treatments and other numerical schemes to further increase its robustness and versatility.

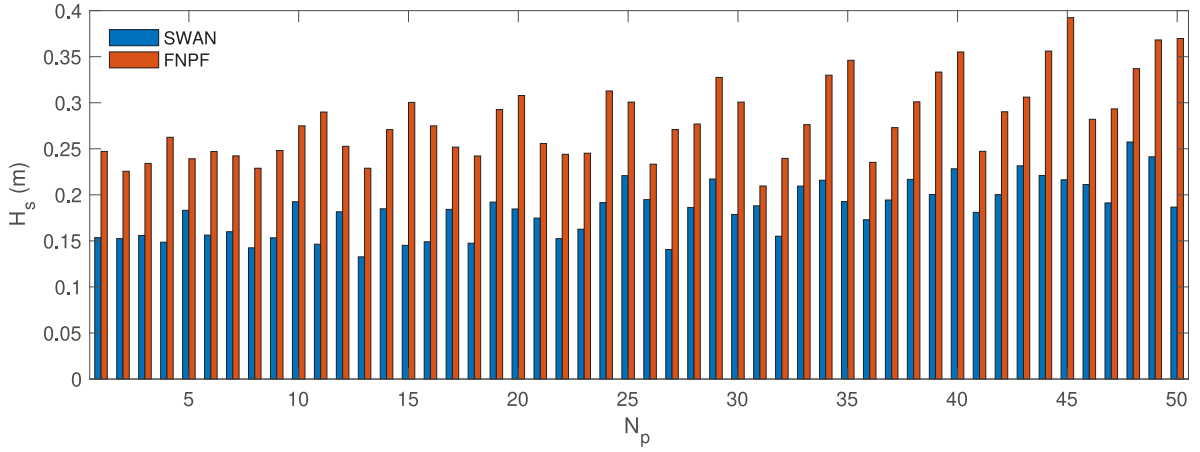


Fig. 41. Comparison of H_s at all wave gauges between SWANN and REEF3D::FNPF in the simulations of wave propagation in Flatøya.

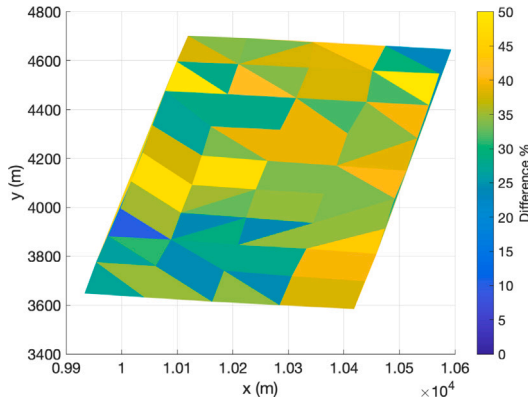


Fig. 42. Differences of H_s in percentage at all wave gauges between SWAN and REEF3D::FNPF simulations at Flatøya.

Declaration of competing interest

The authors declare that they have no known competing financial interests or personal relationships that could have appeared to influence the work reported in this paper.

Acknowledgements

This study has been carried out as part of the E39 fjord crossing project (No. 304624) and the authors are grateful for the grants provided by the Norwegian Public Roads Administration. The computations were performed on resources provided by UNINETT Sigma2 — the National Infrastructure for High-Performance Computing and Data Storage in Norway. The authors are grateful to the model test data provided by the Transnational Access to Research Infrastructures Program of the European Commission under the contract HPRI-CT-2001-00176. The bi-chromatic wave data has been collected in SINTEF Ocean's basin during a research project supported by The Research Council of Norway. The authors are also grateful for the grants 245956 and 269870 provided under the FORINFRA Program (Large Scale Infrastructures), Phase II and III. The authors are also grateful for the generous help and data provided by professor Robert Warren Whalin.

Appendix

The gradient terms of the free-surface boundary conditions are discretised with the 5th-order Hamilton–Jacobi version of the weighted essentially non-oscillatory (WENO) scheme (Jiang and Shu, 1996). The

WENO stencil consists of three local essentially non-oscillatory (ENO)-stencils based on the smoothness indicators IS (Jiang and Shu, 1996). A large IS means a non-smooth solution in a local stencil. The scheme is designed such that the local stencil with the highest smoothness (smallest IS) is assigned the largest weight ω_i , and therefore contributes the most significantly. In this way, the scheme is able to handle large gradients up to shock with good accuracy. The WENO approximation for Φ is a convex combination of the three possible ENO approximations. For example, in the x -direction, the discretisation is formulated as the following:

$$\Phi_x^\pm = \omega_1^\pm \Phi_x^{1\pm} + \omega_2^\pm \Phi_x^{2\pm} + \omega_3^\pm \Phi_x^{3\pm}. \quad (32)$$

The three stencils are defined as:

$$\begin{aligned} \Phi_x^\pm &= \frac{1}{3}q_1^\pm - \frac{7}{6}q_2^\pm + \frac{11}{6}q_3^\pm, \\ \Phi_x^\pm &= -\frac{1}{6}q_2^\pm + \frac{5}{6}q_3^\pm + \frac{1}{3}q_4^\pm, \\ \Phi_x^\pm &= \frac{1}{3}q_3^\pm + \frac{5}{6}q_4^\pm - \frac{1}{6}q_5^\pm. \end{aligned} \quad (33)$$

with

$$\begin{aligned} q_1^- &= \frac{\Phi_{i-2} - \Phi_{i-3}}{\Delta x}, q_2^- = \frac{\Phi_{i-1} - \Phi_{i-2}}{\Delta x}, q_3^- = \frac{\Phi_i - \Phi_{i-1}}{\Delta x}, \\ q_4^- &= \frac{\Phi_{i+1} - \Phi_i}{\Delta x}, q_5^- = \frac{\Phi_{i+2} - \Phi_{i+1}}{\Delta x} \end{aligned} \quad (34)$$

and

$$\begin{aligned} q_1^+ &= \frac{\Phi_{i+3} - \Phi_{i+2}}{\Delta x}, q_2^+ = \frac{\Phi_{i+2} - \Phi_{i+1}}{\Delta x}, q_3^+ = \frac{\Phi_{i+1} - \Phi_i}{\Delta x}, \\ q_4^+ &= \frac{\Phi_i - \Phi_{i-1}}{\Delta x}, q_5^+ = \frac{\Phi_{i-1} - \Phi_{i-2}}{\Delta x} \end{aligned} \quad (35)$$

The weights are written as

$$\omega_1^\pm = \frac{\alpha_1^\pm}{\alpha_1^\pm + \alpha_2^\pm + \alpha_3^\pm}, \omega_2^\pm = \frac{\alpha_2^\pm}{\alpha_1^\pm + \alpha_2^\pm + \alpha_3^\pm}, \omega_3^\pm = \frac{\alpha_3^\pm}{\alpha_1^\pm + \alpha_2^\pm + \alpha_3^\pm} \quad (36)$$

and

$$\alpha_1^\pm = \frac{1}{10} \frac{1}{(\tilde{\epsilon} + IS_1^\pm)^2}, \alpha_2^\pm = \frac{6}{10} \frac{1}{(\tilde{\epsilon} + IS_2^\pm)^2}, \alpha_3^\pm = \frac{3}{10} \frac{1}{(\tilde{\epsilon} + IS_3^\pm)^2} \quad (37)$$

with the regularisation parameter $\tilde{\epsilon} = 10^{-6}$ and the following smoothness indicators:

$$\begin{aligned} IS_1^\pm &= \frac{13}{12} (q_1 - 2q_2 + q_3)^2 + \frac{1}{4} (q_1 - 4q_2 + 3q_3)^2, \\ IS_2^\pm &= \frac{13}{12} (q_2 - 2q_3 + q_4)^2 + \frac{1}{4} (q_2 - q_4)^2, \\ IS_3^\pm &= \frac{13}{12} (q_3 - 2q_4 + q_5)^2 + \frac{1}{4} (3q_3 - 4q_4 + q_5)^2, \end{aligned} \quad (38)$$

References

- Aggarwal, A., Bihs, H., Shirinov, S., Myrhaug, D., 2019. Estimation of breaking wave properties and their interaction with a jacket structure. *J. Fluids Struct.* (ISSN: 0889-9746) 91, 102722. <http://dx.doi.org/10.1016/j.jfluidstruct.2019.102722>.
- Aggarwal, A., Tomaselli, P.D., Christensen, E.D., Bihs, H., 2020. Computational fluid dynamics investigations of breaking focused wave-induced loads on a monopile and the effect of breaker location. *J. Offshore Mech. Arctic Eng.* (ISSN: 0892-7219) 142, 2. <http://dx.doi.org/10.1115/1.4045187>.
- Ahmad, N., Bihs, H., Myrhaug, D., Kamath, A., Arntsen, Ø.A., 2019. Numerical modeling of breaking wave induced seawall scour. *Coast. Eng.* (ISSN: 0378-3839) 150, 108–120. <http://dx.doi.org/10.1016/j.coastaleng.2019.03.010>.
- Ahmad, N., Kamath, A., Bihs, H., 2020. 3D numerical modelling of scour around a jacket structure with dynamic free surface capturing. *Ocean Eng.* (ISSN: 0029-8018) 200, 107104. <http://dx.doi.org/10.1016/j.oceaneng.2020.107104>.
- Alagan Chella, M., Bihs, H., Kamath, A., Myrhaug, D., Arntsen, Ø.A., 2019. Breaking wave interaction with a group of four vertical slender cylinders in two square arrangements. *J. Offshore Mech. Arctic Eng.* (ISSN: 0892-7219) 141, 6. <http://dx.doi.org/10.1115/1.4043597>.
- Alagan Chella, M., Bihs, H., Myrhaug, D., Muskulus, M., 2017. Breaking solitary waves and breaking wave forces on a vertically mounted slender cylinder over an impermeable sloping seabed. *J. Ocean Eng. Mar. Energy* (ISSN: 2198-6452) 3 (1), 1–19. <http://dx.doi.org/10.1007/s40722-016-0055-5>.
- Baquet, A., Kim, J., Huang, Z.J., 2017. Numerical modeling using CFD and potential wave theory for three-hour nonlinear irregular wave simulations. In: International Conference on Offshore Mechanics and Arctic Engineering. Vol. 1: Offshore Technology, V001T01A002. <http://dx.doi.org/10.1115/OMAE2017-61090>.
- Beji, S., Battjes, J., 1993. Experimental investigation of wave propagation over a bar. *Coast. Eng.* (ISSN: 0378-3839) 19 (1), 151–162. [http://dx.doi.org/10.1016/0378-3839\(93\)90022-Z](http://dx.doi.org/10.1016/0378-3839(93)90022-Z).
- Bihs, H., Kamath, A., Alagan Chella, M., Aggarwal, A., Arntsen, Ø.A., 2016. A new level set numerical wave tank with improved density interpolation for complex wave hydrodynamics. *Comput. Fluids* (ISSN: 0045-7930) 140, 191–208. <http://dx.doi.org/10.1016/j.compfluid.2016.09.012>.
- Bihs, H., Wang, W., Pákozdi, C., Kamath, A., 2020. REEF3D:FNFP-A flexible fully nonlinear potential flow solver. *J. Offshore Mech. Arctic Eng.* (ISSN: 0892-7219) 142, 041902. <http://dx.doi.org/10.1115/1.4045915>.
- Bingham, H.B., Zhang, H., 2007. On the accuracy of finite-difference solutions for nonlinear water waves. *J. Eng. Math.* (ISSN: 1573-2703) 58 (1), 211–228. <http://dx.doi.org/10.1007/s10665-006-9108-4>.
- Bonnefoy, F., Touzé, D.L., Ferrant, P., 2006a. A fully-spectral 3D time-domain model for second-order simulation of wavetank experiments. Part A: Formulation, implementation and numerical properties. *Appl. Ocean Res.* (ISSN: 0141-1187) 28 (1), 33–43. <http://dx.doi.org/10.1016/j.apor.2006.05.004>.
- Bonnefoy, F., Touzé, D.L., Ferrant, P., 2006b. A fully-spectral 3D time-domain model for second-order simulation of wavetank experiments. Part B: Validation, calibration versus experiments and sample applications. *Appl. Ocean Res.* (ISSN: 0141-1187) 28 (2), 121–132. <http://dx.doi.org/10.1016/j.apor.2006.05.003>.
- Booij, N., Ris, R.C., Holthuijsen, L.H., 1999. A third-generation wave model for coastal regions. 1. Model description and validation. *J. Geophys. Res.* 104, 7649–7666.
- Chen, W., Panchang, V., Demirebilek, Z., 2005. On the modeling of wave-current interaction using the elliptic mild-slope wave equation. *Ocean Eng.* (ISSN: 0029-8018) 32 (17), 2135–2164. <http://dx.doi.org/10.1016/j.oceaneng.2005.02.010>.
- Clamond, D., Dutykh, D., 2018. Accurate fast computation of steady two-dimensional surface gravity waves in arbitrary depth. *J. Fluid Mech.* 844, 491–518. <http://dx.doi.org/10.1017/jfm.2018.208>.
- Derakhti, M., Kirby, J.T., Banner, M.L., Grilli, S.T., Thomson, J., 2020. A unified breaking onset criterion for surface gravity water waves in arbitrary depth. *J. Geophys. Res.* 125 (7), e2019JC015886. <http://dx.doi.org/10.1029/2019JC015886>.
- Derakhti, M., Kirby, J.T., Shi, F., Ma, G., 2016a. NHWAVE: Consistent boundary conditions and turbulence modeling. *Ocean Modell.* (ISSN: 1463-5003) 106, 121–130. <http://dx.doi.org/10.1016/j.oceanmod.2016.09.002>.
- Derakhti, M., Kirby, J.T., Shi, F., Ma, G., 2016b. Wave breaking in the surf zone and deep-water in a non-hydrostatic RANS model. Part 1: Organized wave motions. *Ocean Modell.* (ISSN: 1463-5003) 107, 125–138. <http://dx.doi.org/10.1016/j.oceanmod.2016.09.001>.
- Derakhti, M., Kirby, J.T., Shi, F., Ma, G., 2016c. Wave breaking in the surf zone and deep-water in a non-hydrostatic RANS model. Part 2: Turbulence and mean circulation. *Ocean Modell.* (ISSN: 1463-5003) 107, 139–150. <http://dx.doi.org/10.1016/j.oceanmod.2016.09.011>.
- DNV-GL, 2011. Modelling and Analysis of Marine Operations. DNV-RP-H103, Det Norske Veritas - Germanischer Lloyd, Veritasveien 1, Høvik, Norway.
- Ducrozet, G., Bonnefoy, F., Touzé, D.L., Ferrant, P., 2012. A modified high-order spectral method for wavemaker modeling in a numerical wave tank. *Eur. J. Mech. B Fluids* (ISSN: 0997-7546) 34, 19–34. <http://dx.doi.org/10.1016/j.euromechflu.2012.01.017>.
- Engsig-Karup, A.P., Bingham, H.B., Lindberg, O., 2009. An efficient flexible-order model for 3D nonlinear water waves. *J. Comput. Phys.* (ISSN: 0021-9991) 228 (6), 2100–2118. <http://dx.doi.org/10.1016/j.jcp.2008.11.028>.
- Engsig-Karup, A., Glimberg, S., Nielsen, A., Lindberg, O., 2013. Fast hydrodynamics on heterogeneous many-core hardware. In: Couturier, R. (Ed.), *Designing Scientific Applications on GPUs*. Taylor & Francis, ISBN: 978-1-4665-7162-4, pp. 251–294.
- Engsig-Karup, A.P., Madsen, M.G., Glimberg, S.L., 2012. A massively parallel GPU-accelerated model for analysis of fully nonlinear free surface waves. *Int. J. Numer. Methods Fluids* 70 (1), 20–36.
- Fenton, J.D., 1985. A fifth-order Stokes theory for steady waves. *J. Waterw. Port Coast. Ocean Eng.* 111 (2), 216–234.
- Fructus, D., Clamond, D., Grue, J., Kristiansen, Ø., 2005. An efficient model for three-dimensional surface wave simulations: Part I: Free space problems. *J. Comput. Phys.* (ISSN: 0021-9991) 205 (2), 665–685. <http://dx.doi.org/10.1016/j.jcp.2004.11.027>.
- Glimberg, S.L., Engsig-Karup, A.P., Nielsen, A.S., Dammann, B., 2013. Development of software components for heterogeneous many-core architectures. In: Couturier, R. (Ed.), *Designing Scientific Applications on GPUs*. In: *Lecture Notes in Computational Science and Engineering*, CRC Press / Taylor & Francis Group, pp. 73–104.
- Glimberg, S.L., Engsig-Karup, A.P., Olson, L.N., 2019. A massively scalable distributed multigrid framework for nonlinear marine hydrodynamics. *Int. J. High Perform. Comput. Appl.* 33 (5), 855–868. <http://dx.doi.org/10.1177/1094342019826662>.
- Gobbi, M.F., Kirby, J.T., Wei, G., 2000. A fully nonlinear Boussinesq model for surface waves. Part 2. Extension to $O(kh)^4$. *J. Fluid Mech.* 405, 181–210. <http://dx.doi.org/10.1017/S0022112099007247>.
- Grilli, S.T., Guyenne, P., Dias, F., 2001. A fully non-linear model for three-dimensional overturning waves over an arbitrary bottom. *Int. J. Numer. Methods Fluids* 35 (7), 829–867. [http://dx.doi.org/10.1002/1097-0363\(20010415\)35:7<829::AID-FLD115>3.0.CO;2-2](http://dx.doi.org/10.1002/1097-0363(20010415)35:7<829::AID-FLD115>3.0.CO;2-2).
- Grilli, S.T., Horrillo, J., 1997. Numerical generation and absorption of fully nonlinear periodic waves. *J. Eng. Mech.* 123 (10), 1060–1069. [http://dx.doi.org/10.1061/\(ASCE\)0733-9399\(1997\)123:10\(1060\)](http://dx.doi.org/10.1061/(ASCE)0733-9399(1997)123:10(1060)).
- Grilli, S.T., Horrillo, J., Guignard, S., 2020a. Fully nonlinear potential flow simulations of wave shoaling over slopes: spilling breaker model and integral wave properties. *Water Waves* (ISSN: 2523-3688) 2 (2), 263–297. <http://dx.doi.org/10.1007/s42286-019-00017-6>.
- Grilli, S.T., Subramanya, R., 1996. Numerical modeling of wave breaking induced by fixed or moving boundaries. *Comput. Mech.* (ISSN: 1432-0924) 17 (6), 374–391. <http://dx.doi.org/10.1007/BF00363981>.
- Grilli, S.T., Subramanya, R., Svendsen, I.A., Veeramony, J., 1994. Shoaling of solitary waves on plane beaches. *J. Waterw. Port Coast. Ocean Eng.* 120 (6), 609–628.
- Grilli, A.R., Westcott, G., Grilli, S.T., Spaulding, M.L., Shi, F., Kirby, J.T., 2020b. Assessing coastal hazard from extreme storms with a phase resolving wave model: Case study of Narragansett, RI, USA. *Coast. Eng.* (ISSN: 0378-3839) 160, 103735. <http://dx.doi.org/10.1016/j.coastaleng.2020.103735>.
- Hagen, L., 2015. *Bunddata-Multistrå Lekkolodd*. Tech. Rep., Aqua Kompetanse AS.
- Holthuijsen, L., Herman, A., Booij, N., 2003. Phase-decoupled refraction-diffraction for spectral wave models. *Coast. Eng.* (ISSN: 0378-3839) 49 (4), 291–305. [http://dx.doi.org/10.1016/S0378-3839\(03\)00065-6](http://dx.doi.org/10.1016/S0378-3839(03)00065-6).
- Jensen, J.H., Madsen, E.Ø., Fredsøe, J., 1999. Oblique flow over dredged channels. II: Sediment transport and morphology. *J. Hydraul. Eng.* 125 (11), 1190–1198. [http://dx.doi.org/10.1061/\(ASCE\)0733-9429\(1999\)125:11\(1190\)](http://dx.doi.org/10.1061/(ASCE)0733-9429(1999)125:11(1190)).
- Jeschke, A., Pedersen, G.K., Vater, S., Behrens, J., 2017. Depth-averaged non-hydrostatic extension for shallow water equations with quadratic vertical pressure profile: equivalence to Boussinesq-type equations. *Int. J. Numer. Methods Fluids* 84 (10), 569–583. <http://dx.doi.org/10.1002/fld.4361>.
- Jiang, G.S., Shu, C.W., 1996. Efficient implementation of weighted ENO schemes. *J. Comput. Phys.* 126, 202–228.
- Kamath, A., Alagan Chella, M., Bihs, H., Arntsen, Ø.A., 2016. Breaking wave interaction with a vertical cylinder and the effect of breaker location. *Ocean Eng.* (ISSN: 0029-8018) 128, 105–115. <http://dx.doi.org/10.1016/j.oceaneng.2016.10.025>.
- Kirby, J.T., Wei, G., Chen, Q., Kennedy, A.B., Dalrymple, R.A., 1998. FUNWAVE 1.0 Fully Nonlinear Boussinesq Wave Model Documentation and User's Manual. Tech. Rep., Center for Applied Coastal Research, Department of Civil Engineering, University of Delaware, Newark.
- Larsen, J., Dancy, H., 1983. Open boundaries in short wave simulations — A new approach. *Coast. Eng.* (ISSN: 0378-3839) 7 (3), 285–297. [http://dx.doi.org/10.1016/0378-3839\(83\)90022-4](http://dx.doi.org/10.1016/0378-3839(83)90022-4).
- Le Méhauté, B., 1976. *An Introduction to Hydrodynamics and Water Waves*. Springer-Verlag, New York.
- Li, B., Fleming, C.A., 1997. A three dimensional multigrid model for fully nonlinear water waves. *Coast. Eng.* (ISSN: 0378-3839) 30 (3), 235–258. [http://dx.doi.org/10.1016/S0378-3839\(96\)00046-4](http://dx.doi.org/10.1016/S0378-3839(96)00046-4).
- Lynett, P.J., 2006. Nearshore wave modeling with high-order Boussinesq-type equations. *J. Waterw. Port Coast. Ocean Eng.* 132 (5), 348–357. [http://dx.doi.org/10.1061/\(ASCE\)0733-950X\(2006\)132:5\(348\)](http://dx.doi.org/10.1061/(ASCE)0733-950X(2006)132:5(348)).
- Lynett, P., Liu, P.L.-F., 2004. A two-layer approach to wave modelling. *Proc. R. Soc. Lond. Ser. A Math. Phys. Eng. Sci.* 460 (2049), 2637–2669. <http://dx.doi.org/10.1098/rspa.2004.1305>.
- Lynett, P.J., Swigler, D., Son, S., Bryant, D., Socolofsky, S., 2011. Experimental study of solitary wave evolution over a 3D shallow shelf. *Coast. Eng. Proc.* 1 (32), currents.1. <http://dx.doi.org/10.9753/icce.v32.currents.1>.
- Ma, G., Shi, F., Kirby, J.T., 2012. Shock-capturing non-hydrostatic model for fully dispersive surface wave processes. *Ocean Modell.* (ISSN: 1463-5003) 43-44, 22–35. <http://dx.doi.org/10.1016/j.oceanmod.2011.12.002>.

- Madsen, P.A., Bingham, H.B., Liu, H., 2002. A new Boussinesq method for fully nonlinear waves from shallow to deep water. *J. Fluid Mech.* 462, 1–30.
- Madsen, P.A., Murray, R., Sørensen, O.R., 1991. A new form of the Boussinesq equations with improved linear dispersion characteristics. *Coast. Eng.* 15, 371–388.
- Madsen, P.A., Schäffer, H.A., 1998. Higher-order Boussinesq-type equations for surface gravity waves: derivation and analysis. *Philos. Trans. R. Soc. Lond. Ser. A Math. Phys. Eng. Sci.* 356 (1749), 3123–3181. <http://dx.doi.org/10.1098/rsta.1998.0309>.
- Madsen, P.A., Sørensen, O.R., 1992. A new form of the Boussinesq equations with improved linear dispersion characteristics. Part 2. A slowly-varying bathymetry. *Coast. Eng.* (ISSN: 0378-3839) 18 (3), 183–204. [http://dx.doi.org/10.1016/0378-3839\(92\)90019-Q](http://dx.doi.org/10.1016/0378-3839(92)90019-Q).
- Martin, T., Kamath, A., Bihs, H., 2020. A Lagrangian approach for the coupled simulation of fixed net structures in a Eulerian fluid model. *J. Fluids Struct.* (ISSN: 0889-9746) 94, 102962. <http://dx.doi.org/10.1016/j.jfluidstructs.2020.102962>.
- Mayer, S., Garapon, A., Sørensen, L.S., 1998. A fractional step method for unsteady free surface flow with applications to non-linear wave dynamics. *Int. J. Numer. Methods Fluids* 28, 293–315.
- Monteban, D., 2016. Numerical Modelling of Wave Agitation in Ports and Access Channels (Master's thesis). Delft University of Technology, Delft, the Netherlands.
- Nwogu, O., 1993. Alternative form of Boussinesq equations for nearshore wave propagation. *J. Waterw. Port Coast. Ocean Eng.* 119 (6), 618–638.
- Osher, S., Sethian, J.A., 1988. Fronts propagating with curvature-dependent speed: algorithms based on Hamilton-Jacobi formulations. *J. Comput. Phys.* 79, 12–49.
- Pákozdi, C., Wang, W., Bihs, H., Fouques, S., 2019. Validation of a high-performance computing nonlinear potential theory based numerical wave tank for wave structure interaction. In: *Proceedings of the Coastal Structures Conference 2019*. pp. 127–137.
- Pákozdi, C., Wang, W., Kamath, A., Bihs, H., 2021. Reduction of the wave propagation error of a sigma grid based numerical tank using a vertical spacing based on the constant truncation error. *Ocean Eng.* (ISSN: 0029-8018) 239, 109741. <http://dx.doi.org/10.1016/j.oceaneng.2021.109741>.
- Peng, D., Merriman, B., Osher, S., Zhao, H., Kang, M., 1999. A PDE-based fast local level set method. *J. Comput. Phys.* 155, 410–438.
- Raoult, C., Benoit, M., Yates, M.L., 2016. Validation of a fully nonlinear and dispersive wave model with laboratory non-breaking experiments. *Coast. Eng.* (ISSN: 0378-3839) 114, 194–207. <http://dx.doi.org/10.1016/j.coastaleng.2016.04.003>.
- Ris, R.C., Booij, N., Holthuijsen, L.H., 1999. A third-generation wave model for coastal regions 2. Verification. *J. Geophys. Res.* 104, 7667–7681.
- Sasikumar, A., Kamath, A., Bihs, H., 2020. Modeling porous coastal structures using a level set method based VRANS-solver on staggered grids. *Coast. Eng. J.* 62 (2), 198–216. <http://dx.doi.org/10.1080/21664250.2020.1734412>.
- Shi, F., Kirby, J.T., Harris, J.C., Geiman, J.D., Grilli, S.T., 2012. A high-order adaptive time-stepping TVD solver for boussinesq modeling of breaking waves and coastal inundation. *Ocean Modell.* (ISSN: 1463-5003) 43-44, 36–51. <http://dx.doi.org/10.1016/j.ocemod.2011.12.004>.
- Shu, C.W., Osher, S., 1988. Efficient implementation of essentially non-oscillatory shock capturing schemes. *J. Comput. Phys.* 77, 439–471.
- Simon, B., Papoutsellis, C.E., Benoit, M., Yates, M.L., 2019. Comparing methods of modeling depth-induced breaking of irregular waves with a fully nonlinear potential flow approach. *J. Ocean Eng. Mar. Energy* (ISSN: 2198-6452) 5 (4), 365–383. <http://dx.doi.org/10.1007/s40722-019-00154-7>.
- Smit, P., Zijlema, M., Stelling, G., 2013. Depth-induced wave breaking in a non-hydrostatic, near-shore wave model. *Coast. Eng.* (ISSN: 0378-3839) 76, 1–16. <http://dx.doi.org/10.1016/j.coastaleng.2013.01.008>.
- Stansby, P.K., Zhou, J.G., 1998. Shallow-water flow solver with non-hydrostatic pressure: 2D vertical plane problems. *Int. J. Numer. Methods Fluids* 28 (3), 541–563. [http://dx.doi.org/10.1002/\(SICI\)1097-0363\(19980915\)28:3<541::AID-FLD738>3.0.CO;2-O](http://dx.doi.org/10.1002/(SICI)1097-0363(19980915)28:3<541::AID-FLD738>3.0.CO;2-O).
- Statens kartverk, 2020. Aero image of Norway. <https://www.norgeskart.no>, last accessed on 5/4/2020.
- Stelling, G.S., Duinmeijer, S.P.A., 2003. A staggered conservative scheme for every Froude number in rapidly varied shallow water flows. *Int. J. Numer. Methods Fluids* 43 (12), 1329–1354. <http://dx.doi.org/10.1002/flid.537>.
- Sussman, M., Smereka, P., Osher, S., 1994. A level set approach for computing solutions to incompressible two-phase flow. *J. Comput. Phys.* 114, 146–159.
- SWAN, 2016. *Swan User Manual*. 2600 GA Delft, The Netherlands.
- Thomas, T.J., Dwarakish, G., 2015. Numerical wave modelling—a review. *Aquat. Procedia* (ISSN: 2214-241X) 4, 443–448. <http://dx.doi.org/10.1016/j.aqpro.2015.02.059>.
- Ting, F.C.K., Kirby, J.T., 1995. Dynamics of surf-zone turbulence in a strong plunging breaker. *Coast. Eng.* 24, 177–204.
- van der Vorst, H., 1992. BiCGStab: a fast and smoothly converging variant of Bi-CG for the solution of nonsymmetric linear systems. *SIAM J. Sci. Comput.* 13, 631–644.
- van Groesen, E., Andonowati, 2007. Variational derivation of KdV-type models for surface water waves. *Phys. Lett. A* (ISSN: 0375-9601) 366 (3), 195–201. <http://dx.doi.org/10.1016/j.physleta.2007.02.031>.
- van Groesen, E., Andonowati, She Liam, L., Lakhturov, I., 2010. Accurate modelling of uni-directional surface waves. *J. Comput. Appl. Math.* (ISSN: 0377-0427) 234 (6), 1747–1756. <http://dx.doi.org/10.1016/j.cam.2009.08.024>, Eighth International Conference on Mathematical and Numerical Aspects of Waves (Waves 2007).
- Vold, S., Lothe, A.E., 2009. Mehamn - Modellforsk. Tech. Rep. SBF IN F09203, SINTEF Byggeforsk, Trondheim.
- Wang, W., Kamath, A., Martin, T., Pákozdi, C., Bihs, H., 2020a. A comparison of different wave modelling techniques in an open-source hydrodynamic framework. *J. Mar. Sci. Eng.* (ISSN: 2077-1312) 8, 7. <http://dx.doi.org/10.3390/jmse8070526>.
- Wang, W., Kamath, A., Pákozdi, C., Bihs, H., 2019. Investigation of focusing wave properties in a numerical wave tank with a fully nonlinear potential flow model. *J. Mar. Sci. Eng.* (ISSN: 2077-1312) 7 (10), 375. <http://dx.doi.org/10.3390/jmse7100375>.
- Wang, W., Martin, T., Kamath, A., Bihs, H., 2020b. An improved depth-averaged nonhydrostatic shallow water model with quadratic pressure approximation. *Int. J. Numer. Methods Fluids* 92 (8), 803–824. <http://dx.doi.org/10.1002/flid.4807>.
- Warren, I., Bach, H., 1992. MIKE 21: a modelling system for estuaries, coastal waters and seas. *Environ. Softw.* (ISSN: 0266-9838) 7 (4), 229–240. [http://dx.doi.org/10.1016/0266-9838\(92\)90006-P](http://dx.doi.org/10.1016/0266-9838(92)90006-P), 3rd International Software Exhibition for Environmental Science and Engineering.
- Wei, G., Kirby, J.T., Grilli, S.T., Subramanya, R., 1995. A fully nonlinear Boussinesq model for surface waves. Part 1. Highly nonlinear unsteady waves. *J. Fluid Mech.* 294, 71–92. <http://dx.doi.org/10.1017/S0022112095002813>.
- Whalin, R., 1971. The Limit of Applicability of Linear Wave Refraction Theory in a Convergence Zone, Research Report H-71-3. Tech. Rep., U.S. Army Corps of Engineers.
- Yates, M.L., Benoit, M., 2015. Accuracy and efficiency of two numerical methods of solving the potential flow problem for highly nonlinear and dispersive water waves. *Int. J. Numer. Methods Fluids* 77 (10), 616–640. <http://dx.doi.org/10.1002/flid.3992>.
- Zhang, J., Benoit, M., Kimmoun, O., Chabchoub, A., Hsu, H.-C., 2019. Statistics of extreme waves in coastal waters: large scale experiments and advanced numerical simulations. *Fluids* 4 (2), 99. <http://dx.doi.org/10.3390/fluids4020099>.
- Zhou, J., Stansby, P., 1999. An arbitrary Lagrangian-Eulerian σ (ALES) model with non-hydrostatic pressure for shallow water flows. *Comput. Methods Appl. Mech. Eng.* (ISSN: 0045-7825) 178 (1), 199–214. [http://dx.doi.org/10.1016/S0045-7825\(99\)00014-6](http://dx.doi.org/10.1016/S0045-7825(99)00014-6).
- Zijlema, M., Stelling, G.S., 2005. Further experiences with computing non-hydrostatic free-surface flows involving water waves. *Int. J. Numer. Methods Fluids* 48 (2), 169–197. <http://dx.doi.org/10.1002/flid.821>.
- Zijlema, M., Stelling, G., 2008. Efficient computation of surf zone waves using the nonlinear shallow water equations with non-hydrostatic pressure. *Coast. Eng.* (ISSN: 0378-3839) 55 (10), 780–790. <http://dx.doi.org/10.1016/j.coastaleng.2008.02.020>.
- Zijlema, M., Stelling, G., Smit, P., 2011. SWASH: An operational public domain code for simulating wave fields and rapidly varied flows in coastal waters. *Coast. Eng.* (ISSN: 0378-3839) 58 (10), 992–1012. <http://dx.doi.org/10.1016/j.coastaleng.2011.05.015>.